Received 25 May 2023; revised 21 June 2023; accepted 2 July 2023. Date of publication 12 July 2023; date of current version 27 July 2023.

Digital Object Identifier 10.1109/OJCOMS.2023.3292796

Deterministic Algorithms for Four-Dimensional Imaging in Colocated MIMO OFDM-Based Radar Systems

MICHELE MIRABELLA [1,2] (Graduate Student Member, IEEE), PASQUALE DI VIESTI [1,2] (Graduate Student Member, IEEE), AND GIORGIO M. VITETTA [1,2] (Senior Member, IEEE)

[1]Department of Engineering "Enzo Ferrari," University of Modena and Reggio Emilia, 41125 Modena, Italy

[2]Consorzio Nazionale Interuniversitario per le Telecomunicazioni (CNIT), 43124 Parma, Italy

CORRESPONDING AUTHOR: M. MIRABELLA (e-mail: michele.mirabella@unimore.it)

ABSTRACT In this manuscript, the problem of detecting multiple targets and jointly estimating their spatial coordinates (namely, the range, the Doppler and the direction of arrival of their electromagnetic echoes) in a colocated multiple-input multiple-output radar system employing orthogonal frequency division multiplexing is investigated. It is well known its optimal solution, namely the joint maximum likelihood estimator of an unknown number of targets, is unfeasible because of its huge computational complexity. Moreover, until now, sub-optimal solutions have not been proposed in the technical literature. In this manuscript a novel approach to the development of reduced complexity solutions is illustrated. It is based on the idea of separating angle estimation from range-Doppler estimation, and of exploiting known algorithms for solving these two sub-problems. A detailed analysis of the accuracy and complexity of various detection and estimation methods based on this approach is provided. Our numerical results evidence that one of these methods is able to approach optimal performance in the maximum likelihood sense with a limited computational effort in different scenarios.

INDEX TERMS Dual-function radar-communication, four-dimensional radar imaging, frequency estimation, multiple-input multiple-output radar, orthogonal frequency division multiplexing, radar processing.

I. INTRODUCTION

WIRELESS communication and radar sensing have been advancing independently for many years, even though they share various similarities in terms of both signal processing and system architecture. This consideration and the problem of radio spectrum scarcity have motivated the investigation of a new class of wireless systems, able to accomplish sensing and communication jointly. Various recent research activities in this field have evidenced that *joint communication and sensing* (JCAS) systems can provide significant advantages in terms of device size, power consumption, cost, and spectral efficiency compared to traditional systems in various applications [1]. Different approaches to their development are currently being investigated [2], [3], [4], [5], [6]. In this manuscript we adopt a *communication-centric* approach; this means that radar sensing represents an add-on to the considered wireless communication system. Moreover, we assume that *orthogonal frequency division multiplexing* (OFDM) is employed for both communication and sensing and that our system is equipped with both *transmit* (TX) and *receive* (RX) arrays (i.e., it is of *multiple-input multiple-output*, MIMO, type).

The OFDM modulation format has been adopted in various wireless communication standards, due to its robustness to multipath fading and to its relatively simple synchronization [5]; in addition, its use in MIMO communication systems has been widely investigated (e.g., see [7], [8] and references therein). A wide technical literature on the use of OFDM for radar sensing refers mainly to *single input, single output* (SISO) systems [2], [9], [10], [11], [12], [13], [14], [15], [16]. For this class of systems, various *direct* and *indirect sensing* methods for target detection and estimation have

been proposed. Generally speaking, *direct sensing methods* extract target information from the received signal without compensating for the effect of the data payload it conveys (e.g., see [1], [11], [17]) and typically exploit computationally intensive *compressed sensing* (CS) techniques. An example of application of CS is shown in [18], in which different multiplexing alternatives to OFDM are analyzed and the CS technique is employed to overcome the random assignment of subcarriers. *Indirect estimation methods*, instead, require estimating the communication channel and, consequently, compensating for the contribution due to channel symbols (e.g., see [2, eq. (20)]), which are known at the RX side of any colocated radar. Indirect sensing methods can be divided in: 1) *discrete Fourier transform* (DFT)-based or *correlation-based* methods (i.e., methods based on the *matched filter*, MF, concept) [10], [12], [19]; 2) *subspace* methods [15], [16]; 3) *maximum likelihood* (ML)-based methods [14], [20], [21]. Correlation-based and DFT-based algorithms are conceptually simple and computationally efficient, but can generate poor radar images in the presence of closely spaced targets and/or strong clutter [22]. Moreover, they can be outperformed by subspace methods, like the well-known *multiple signal classification* (MUSIC) algorithm and the *estimation of signal parameters via rotational invariant technique* (ESPRIT) at the price, however, of a significantly larger computational complexity [16]. An estimation accuracy comparable to that of subspace methods is provided by various ML-based algorithms, which also require a significant computational effort; relevant contributions to this field can be found in [14], [20] and [21].

Indirect sensing methods for JCAS MIMO systems employing OFDM are investigated in [4], [6], [17], [23], [24], [25], [26], [27], [28] and can be classified according to the same criteria as defined above for SISO systems. *Correlation*-based or DFT-based methods are developed in [4], [6], [17] and [28]. In particular, an algorithm combining matched filtering for range estimation with a *one-dimensional* (1D)-MUSIC algorithm for both Doppler and azimuth (i.e., *angle of arrival*, AoA) estimation is proposed in [6]. In [4] a *constant false alarm rate* (CFAR) technique is employed to detect multiple targets, whereas the estimation of their range and Doppler is based on a *two-dimensional* (2D) *fast Fourier transform* (FFT); note that in this case the estimation of AoA is ignored and the availability of antenna arrays is beneficial for communication only. In [17] a 2D-FFT technique is exploited to estimate the range of multiple targets and their azimuth, whereas in [28] multiple FFTs are combined with a clutter removal technique to estimate their range, azimuth and Doppler.

Subspace methods are investigated in [23], [24] and [25]. More specifically, in [23] a subspace-based algorithm assisted by CFAR pre-processing is developed to estimate the range, velocity, and azimuth of multiple targets on the basis of a reduced number of samples and without resorting to high-resolution spectral estimation. In [24] the estimation accuracy of the 2D-MUSIC algorithm is assessed for a varying number of available data snapshots, whereas in [25] the use of an augmented beam-space approach is proposed to make the use of 2D-MUSIC and 2D-ESPRIT possible when hybrid digital arrays are used.

Methods based on an ML approach are proposed in [26] and [27]. In particular, the strategy devised in [26] is based on: 1) a preliminary channel estimation; 2) an ML-based technique for the estimation of the range and *direction of arrival* (DoA) of multiple targets. In [27], instead, a 1D technique, based on a systematic phase correction method and leveraging on the *virtual array* concept, is derived for the estimation of the azimuth of a single target. Finally, an hybrid approach, combining DFT-based and subspace methods, is illustrated in [29]. More specifically, channel estimation is accomplished, after DFT-based processing for range estimation, by means of an *amplitude and phase estimation* (APES)-based method; this method, that exploits the presence of *inter-carrier interference* (ICI) to produce a preliminary estimate of target Doppler, is followed by the 1D-MUSIC algorithm for angular estimation and by 1D-FFT processing to generate the final estimate of target Doppler.

It is important to point out that all the methods mentioned above for JCAS MIMO systems represent *partial solutions to the problem of jointly estimating the range, Doppler, azimuth and elevation of multiple targets*, i.e., briefly, to the *four-dimensional* (4D) imaging problem considered in this manuscript. On the one hand, the authors of [4] focus on range and Doppler estimation only; moreover, they develop a correlation-based method, which is employed after channel estimation and time-frequency synchronization in the context of long-range radar processing. On the other hand, the correlation-based or subspace methods proposed in [17], [24], [25] are able to compute accurate estimates of target azimuth only, whereas the other target parameters are ignored (see [24] and [25]) or estimated with limited accuracy, without any refinement process (see [17]). Similar considerations apply to the ML-based method illustrated in [27], since it can provide accurate estimates of the azimuth of multiple targets, but coarse estimates of their range only. These limitations originate from the fact that an acceptable complexity in subspace-based and ML-based methods can be achieved by neglecting (or accepting poor accuracy in) the estimation of a portion of target parameters. These considerations have motivated the work described in this manuscript, which aims at illustrating how a family of novel and computationally efficient sub-optimal methods able to generate accurate 4D radar images in an OFDM-based JCAS system equipped with TX and RX arrays can be developed; therefore, unlike previous research work, this paper aims at providing a full solution to the above mentioned 4D imaging problem. More specifically, the contribution provided by our manuscript is threefold and can be summarized as follows:

1) A *general strategy*, called *Doppler-range-angle estimation with successive compensation* (DRAEC), is proposed for the detection of multiple targets and the estimation of their parameters in a MIMO OFDM-based JCAS system. This

strategy is based on the idea of: a) decoupling the problem of range-Doppler estimation from that of azimuth-elevation estimation; b) employing an algorithm for the estimation of the parameters of 2D complex tones to solve each of these two sub-problems.

2) An *overview* of the algorithms that can be employed for the detection and the estimation of 2D complex tones, and an analysis of their computational complexity are provided. On the one hand, five of these algorithms are known DFT-based estimation techniques, that have been proposed in the technical literature for related applications (namely, for harmonic retrieval [30], [31] or for radar sensing applications [32], [33]). On the other hand, the remaining algorithm, called *extended Lee algorithm* (ELA), is new, even if it can be considered as an extended version of the ML-based 1D algorithm developed in [27]. Note that all these algorithms have been originally proposed to solve estimation problems that are formally different from the ones considered in this manuscript. For this reason, in this manuscript, their use for target range-Doppler estimation and azimuth-elevation estimation according to the DRAEC strategy is illustrated in detail. Moreover, a unified notation is adopted in their description to ease their implementation and the reading of this manuscript.

3) Based on the above-mentioned estimation algorithms, *seven different embodiments* of the DRAEC strategy are proposed and compared in terms of both accuracy and computational complexity. Six of them are based on the known DFT-based estimation techniques mentioned above, whereas the remaining one relies on the CSFDEC algorithm. This allows us to assess how various state-of-the-art algorithms perform in 4D imaging and how large is the computational effort they require.

The remaining part of this manuscript is organized as follows. In Section II, the processing accomplished in a MIMO OFDM-based radar system is summarized and the received signal model adopted in our work is briefly derived. The DRAEC strategy is illustrated in Section III, whereas various estimators of 2D complex tones and their computational complexity are described in Sections IV and V, respectively. Different embodiments of the DRAEC strategy are proposed and compared, in terms of accuracy and complexity, in Section VI. Finally, some conclusions are offered in Section VII.

Notation: Throughout this paper, the following notation is adopted: 1) $(\cdot)^T$ denotes matrix transposition; 2) $(\cdot)^*$ and $(\cdot)^H$ denote complex conjugate and complex conjugate transpose (Hermitian operator), respectively; 3) the symbols $\otimes$, $\odot$, $*$ and $\times$ represent the Kronecker, Hadamard, Khatri-Rao and Cartesian product operators, respectively; 4) $\Re\{x\}$ and $\Im\{x\}$ indicate the real part and the imaginary part, respectively, of the complex variable x; 5) diag($\mathbf{v}$) represents a square diagonal matrix having the elements of the vector $\mathbf{v}$ along its main diagonal; 6) $\mathbf{0}_{M,N}$ denotes the $M \times N$ null matrix; 7) $\mathbf{I}_M$ denotes the order M identity matrix; 8) $\emptyset$ represents the empty set.

II. SYSTEM AND SIGNAL MODELS

This section focuses on the architecture of the MIMO OFDM-based JCAS system considered in our manuscript and on the processing accomplished at its receive side. Our main objectives are deriving the received signal model in the presence of multiple targets and illustrating some essential assumptions on which it relies. The architecture of the considered JCAS system is illustrated in Fig. 1 and has the following essential features:

1) Its transmitter is *colocated* with the receiver; consequently, the receiver has full knowledge of the structure and content of the transmitted signal and of its carrier frequency, and exploits these information for sensing purposes only.

2) It is equipped with a *transmit* (TX) *horizontal uniform linear array* (HULA) and a *receive* (RX) *vertical uniform linear array* (VULA), consisting of N_T and N_R elements, respectively. All the antennas are placed on the same planar shield, so that a 2D reference system lying on the plane of the physical antenna array can be defined, as illustrated in Fig. 2 (where λ denotes the wavelength of the transmitted signal).

3) The data frames it transmits are made of M consecutive OFDM symbols, each consisting of N subcarriers. Such symbols can convey both pilot tones (for channel estimation and synchronization) and information data to be sent to a single or multiple receivers at different locations.

In our work, each couple of *physical* TX and RX antennas is replaced by a single *virtual antenna* (VA); the abscissa $x_{\mathrm{v}}^{(p,q)}$ and the ordinate $y_{\mathrm{v}}^{(p,q)}$ of the VA element associated with the pth TX antenna and the qth RX antenna (briefly, the (p, q) VA) are evaluated as (e.g., see [34, eqs. (1)–(2)])

$$x_{\mathrm{v}}^{(p,q)} = \left(x_{\mathrm{t}}^{(p)} + x_{\mathrm{r}}^{(q)}\right)/2 \tag{1}$$

and

$$y_{\mathrm{v}}^{(p,q)} = \left(y_{\mathrm{t}}^{(p)} + y_{\mathrm{r}}^{(q)}\right)/2, \tag{2}$$

respectively, with $p = 0, 1, \ldots, N_T - 1$ and $q = 0, 1, \ldots, N_R - 1$; here, $(x_{\mathrm{t}}^{(p)}, y_{\mathrm{t}}^{(p)})$ and $(x_{\mathrm{r}}^{(q)}, y_{\mathrm{r}}^{(q)})$ denote the coordinates of the pth TX and qth RX antenna, respectively. It is easy to show that the set of $N_{\mathrm{VA}} = N_T N_R$ VAs associated with the physical arrays shown in Fig. 2 forms a virtual *uniform rectangular array* (URA). Moreover, based on (1) and (2), the abscissa and ordinate of the VA (p, q) are

$$x_{\mathrm{v}}^{(p,q)} = x_{\mathrm{v}}^{(p)} = \left(x_{\mathrm{t}}^{(0)} + x_{\mathrm{r}}^{(0)} + p\, d_{\mathrm{t}}\right)/2 \tag{3}$$

and

$$y_{\mathrm{v}}^{(p,q)} = y_{\mathrm{v}}^{(q)} = \left(y_{\mathrm{t}}^{(0)} + y_{\mathrm{r}}^{(0)} + q\, d_{\mathrm{r}}\right)/2, \tag{4}$$

respectively; here, $(x_{\mathrm{t}}^{(0)}, y_{\mathrm{t}}^{(0)})$ $(x_{\mathrm{r}}^{(0)}, y_{\mathrm{r}}^{(0)})$ represent the coordinates of the leftmost TX (lowermost RX) antenna and d_{t} (d_{r}) denotes the distance between adjacent antennas of the TX (RX) array (see Fig. 2, where it is assumed that $d_{\mathrm{t}} = d_{\mathrm{r}} = \lambda/2$).

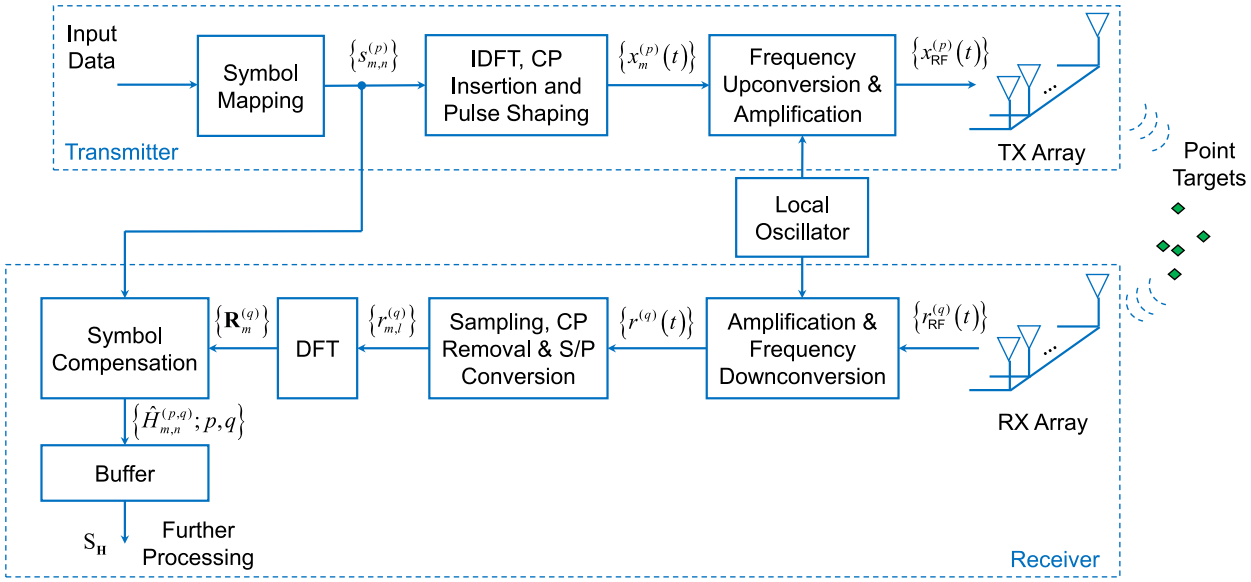

FIGURE 1. Architecture of the considered MIMO OFDM-based JCAS system.

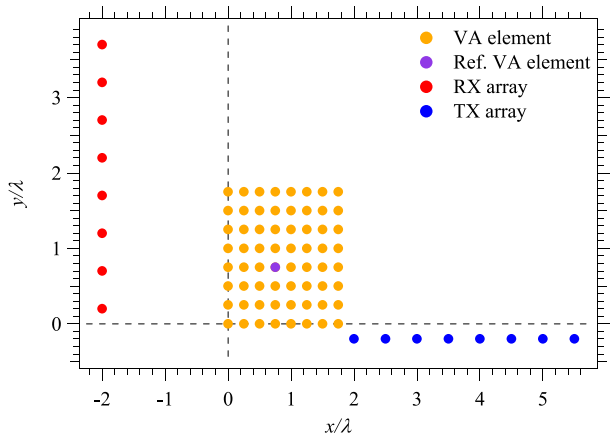

FIGURE 2. Representation of the physical TX and RX arrays, and of the corresponding virtual array characterizing the considered JCAS system. The reference virtual antenna element (corresponding to the couple (p, q)=(4, 4) is identified by a purple circle).

In the following derivations, we concentrate on the transmission of a single frame. The complex envelope of the *radio frequency* (RF) signal conveying the mth OFDM symbol radiated by the pth TX antenna (with $p = 0, 1, \ldots, N_T - 1$) can be expressed as (e.g., see [14, eq. (3)])

$$x_m^{(p)}(t) \triangleq q(t - mT_s) \sum_{n=0}^{N-1} s_{m,n}^{(p)} \exp\left(j2\pi n\Delta_f (t - mT_s)\right) \quad (5)$$

up to a transmit delay; here, $q(t)$ is a windowing function, $s_{m,n}^{(p)}$ is the mth channel symbol conveyed by the nth subcarrier and transmitted by the pth TX antenna, $\Delta_f = 1/T$ is the subcarrier spacing, T is the OFDM symbol interval, $T_s \triangleq T + T_G$ is the overall duration of the OFDM symbol and T_G is the *cyclic prefix* interval. Following [14], a rectangular windowing function is adopted, so that $q(t) = 1$ for $t \in [-T_G, T]$ and $q(t) = 0$ elsewhere.

Given the complex envelope (5), the RF waveform radiated by the pth TX antenna in the considered frame can be expressed as

$$x_{\mathrm{RF}}^{(p)}(t) = \Re\left\{\exp(j2\pi f_c\, t) \sum_{m=0}^{M-1} x_m^{(p)}(t)\right\}, \quad (6)$$

where $f_c = c/\lambda$ denotes the frequency of the local oscillator employed in the up-conversion at the TX side and c the speed of light.

Let assume now that $x_{\mathrm{RF}}^{(p)}(t)$ in (6) is reflected by K distinct point targets, and that the kth target (with $k = 0, 1, \cdots, K-1$) is located at the (initial) distance R_k from the transmitter, moves with the radial velocity[1] v_k with respect to it and is characterized by the azimuth (elevation) angle θ_k (ϕ_k). It is not difficult to show that the complex envelope of the RF signal $r_{\mathrm{RF}}^{(q)}(t)$ (see Fig. 1) captured by the qth RX antenna is[2] (e.g., see [14, eqs. (5) and (6)])

$$r^{(q)}(t) = \sum_{k=0}^{K-1} \sum_{p=0}^{N_T-1} \alpha_k^{(p,q)} \exp\left(-j2\pi f_c \tau_k^{(p,q)}\right) \cdot \exp\left(j2\pi f_{D_k} t\right) \sum_{m=0}^{M-1} x_m^{(p)}\left(t - \tau_k^{(p,q)} + \frac{f_{D_k}}{f_c} t\right) + w^{(q)}(t), \quad (7)$$

1. This velocity is positive (negative) if the target approaches (moves away from) the JCAS system.

2. Note that the overall delay that characterizes the echo originating from the kth target depends on all the parameters of the target itself (namely, its range, its velocity and its angular parameters) and changes over time.

where

$$\tau_k^{(p,q)} \triangleq \frac{2}{c}\Big[R_k + x_{\mathrm{v}}^{(p,q)}\sin(\theta_k)\cos(\phi_k) + y_{\mathrm{v}}^{(p,q)}\sin(\phi_k)\Big] \quad (8)$$

and $\alpha_k^{(p,q)}$ are the overall propagation delay and the attenuation, respectively, associated with the kth point target (and observed on the VA (p, q)),

$$f_{D_k} \triangleq 2\frac{v_k}{\lambda} \quad (9)$$

is the Doppler shift due to the motion of the kth target and $w^{(q)}(t)$ is the complex *additive white Gaussian noise* (AWGN) process affecting $r^{(q)}(t)$.

The signal $r^{(q)}(t)$ in (7) undergoes analog-to-digital conversion followed by DFT processing. A simple mathematical model that describes the sequence generated by sampling $r^{(q)}(t)$ in the mth OFDM symbol interval can be derived as follows. Substituting the *right-hand side* (RHS) of (5) in that of (7), extracting the portion associated with the mth OFDM symbol from the resulting expression and substituting t with $t' = t - mT_{\mathrm{s}}$ yields

$$r_m^{(q)}(t') \triangleq \sum_{k=0}^{K-1} D(f_{D_k}, t')\, \nu_m(f_{D_k})\, A(R_k) \cdot Y_{k,m}^{(q)}(t') + w^{(q)}(t'), \quad (10)$$

where

$$D(f, t') \triangleq \exp(j2\pi f t'), \quad (11)$$

$$\nu_m(f) \triangleq \exp(j2\pi f m T_{\mathrm{s}}), \quad (12)$$

$$A(R) \triangleq \exp(-j4\pi f_{\mathrm{c}} R/c), \quad (13)$$

$$Y_{k,m}^{(q)}(t') \triangleq \sum_{p=0}^{N_T-1} \alpha_k^{(p,q)} B^{(p,q)}(\theta_k, \phi_k) \sum_{n=0}^{N-1} s_{m,n}^{(p)} \gamma_n(R_k) \cdot \eta_n^{(p,q)}(\theta_k, \phi_k)\, \xi_n(f_{D_k}, t')\, \zeta_{m,n}(f_{D_k})\, \exp(j2\pi n \Delta_f t'), \quad (14)$$

$$B^{(p,q)}(\theta, \phi) \triangleq \exp\Big(-j4\pi\Big(x_{\mathrm{v}}^{(p,q)}\sin(\theta)\cos(\phi) + y_{\mathrm{v}}^{(p,q)}\sin(\phi)\Big)/\lambda\Big), \quad (15)$$

$$\gamma_n(R) \triangleq \exp(-j4\pi n \Delta_f R/c), \quad (16)$$

$$\eta_n^{(p,q)}(\theta, \phi) \triangleq \exp\Big(-j4\pi n(\Delta_f/f_{\mathrm{c}})\Big(x_{\mathrm{v}}^{(p,q)}\sin(\theta)\cos(\phi) + y_{\mathrm{v}}^{(p,q)}\sin(\phi)\Big)/\lambda\Big), \quad (17)$$

$$\xi_n(f, t') \triangleq \exp(j2\pi n \Delta_f (f/f_{\mathrm{c}})\, t') \quad (18)$$

and

$$\zeta_{m,n}(f) \triangleq \exp\big(j2\pi n \Delta_f (f/f_{\mathrm{c}})\, m T_{\mathrm{s}}\big). \quad (19)$$

Note that: 1) the term $D(f, t')$, in (10), is responsible for the so called *range migration effect* (see [35]) due to the kth target Doppler frequency, whereas $\nu_m(f_{D_k})$ is proportional to both f_{D_k} and the OFDM symbol index m; 2) the phase of $A(R_k)$ in (10) depends on the range R_k only, whereas that of $\gamma_n(R_k)$ in (14) is proportional to both R_k and the subcarrier index n (see (13) and (16), respectively); 3) The terms in (15) and in (17) both depend on the virtual array configuration as well as the target DoA; 4) the term $\xi_n(f_{D_k}, t')$ in (14) produces a time-dependent phase rotation influenced by both the Doppler frequency f_{D_k} and the subcarrier index n (see (18)); 5) the term $\zeta_{m,n}(f_{D_k})$ in (14) introduces a phase rotation depending on both the OFDM symbol index m and the subcarrier index n (see (19)), and accounts for the so-called *intersubcarrier Doppler effect* (e.g., see [14, Sec. II, p. 3]).

It is not difficult to show that sampling $r_m^{(q)}(t')$ (10) at the instant $t_l' \triangleq lT/N$ (i.e., sampling $r^{(q)}(t)$ at the instant $t_l \triangleq t_l' + mT_{\mathrm{s}}$), with $l = 0, 1, \ldots, N-1$, yields[3]

$$r_{m,l}^{(q)} \triangleq r_m^{(q)}(t_l') = \sum_{k=0}^{K-1} D_l(f_{D_k})\, \nu_m(f_{D_k})\, A(R_k) \cdot Y_{k,m,l}^{(q)} + w_l^{(q)}; \quad (20)$$

here, the term $D_l(f) \triangleq \exp(j2\pi f l T/N)$ accounts for the ICI effect due to the range migration,

$$Y_{k,m,l}^{(q)} \triangleq Y_{k,m}^{(q)}(t_l') = \sum_{p=0}^{N_T-1} \alpha_k^{(p,q)} B^{(p,q)}(\theta_k, \phi_k) \sum_{n=0}^{N-1} s_{m,n}^{(p)}\, \gamma_n(R_k) \cdot \eta_n^{(p,q)}(\theta_k, \phi_k)\, \xi_{n,l}(f_{D_k})\, \zeta_{m,n}(f_{D_k}) \exp(j2\pi nl/N), \quad (21)$$

$\xi_{n,l}(f) \triangleq \xi_n(f, t_l')$ and $w_l^{(q)} \triangleq w^{(q)}(t_l')$ is the Gaussian noise affecting $r_{m,l}^{(q)}$ (an AWGN model is assumed for the sequence $\{w_l^{(q)};\ l = 0, 1, \ldots, N-1\}$).

If the target Dopplers $\{f_{D_k}\}$ are sufficiently small and, more precisely, $|f_{D_k}/f_{\mathrm{c}}| \ll 1/(MN)$ for any k, the factors $\xi_{n,l}(f_{D_k})$ and $\zeta_{m,n}(f_{D_k})$ appearing in the RHS of (21) can be neglected; this leads to the simplified signal model

$$r_{m,l}^{(q)} = \sum_{k=0}^{K-1} D_l(f_{D_k})\, \nu_m(f_{D_k})\, A(R_k) \cdot \sum_{p=0}^{N_T-1} \alpha_k^{(p,q)} B^{(p,q)}(\theta_k, \phi_k) \sum_{n=0}^{N-1} s_{m,n}^{(p)} \exp(j2\pi nl/N) \cdot \gamma_n(R_k)\, \eta_n^{(p,q)}(\theta_k, \phi_k) + w_l^{(q)}. \quad (22)$$

The N signal samples acquired in the mth OFDM symbol interval through the qth RX antenna undergo *serial-to-parallel* (S/P) conversion, as shown in Fig. 1; this produces the N-dimensional vector $\mathbf{r}_m^{(q)} \triangleq \Big[r_{m,0}^{(q)}, r_{m,1}^{(q)}, \ldots, r_{m,N-1}^{(q)}\Big]^T$, for which an order N DFT is computed. The nth element of the resulting DFT output vector

$$\mathbf{R}_m^{(q)} \triangleq \Big[R_{m,0}^{(q)}, R_{m,1}^{(q)}, \ldots, R_{m,N-1}^{(q)}\Big]^T \quad (23)$$

can be expressed as

$$R_{m,n}^{(q)} \triangleq \frac{1}{N}\sum_{l=0}^{N-1} r_{m,l}^{(q)} \exp(-j2\pi nl/N)$$

3. Note that the samples associated with the CP are ignored.

$$= \frac{1}{N}\sum_{k=0}^{K-1} D_n(f_{D_k})\, v_m(f_{D_k})\, A(R_k) \sum_{p=0}^{N_T-1} \alpha_k^{(p,q)} \cdot B^{(p,q)}(\theta_k,\phi_k)\, s_{m,n}^{(p)}\, \gamma_n(R_k)\, \eta_n^{(p,q)}(\theta_k,\phi_k) + W_n^{(q)}, \tag{24}$$

where $W_n^{(q)}$ is the AWGN sample affecting the nth subcarrier.

The received signal model expressed by (24) is general, but quite complicated. In our work, a simplified version of it can be employed since:

1) the approximation

$$\eta_n^{(p,q)}(\theta,\phi) \cong 1 \tag{25}$$

is made for any n, since f_c is assumed to be much greater than Δ_f (see (17));

2) it is assumed that, in the transmission of each OFDM symbol, disjoint subsets of the N available subcarriers are assigned to distinct TX antennas.

The last assumption means that the signal radiated by each TX antenna can be represented as the superposition of a set of multiple subcarriers exclusively assigned to that antenna, i.e., briefly, it consists of *private subcarriers* only.[4] Therefore, if $\mathcal{S}_m^{(p)}$ denotes the set collecting the indices of the subcarriers radiated by the pth TX antenna in the mth symbol interval, we have that

$$\mathcal{S}_m^{(p_1)} \cap \mathcal{S}_m^{(p_2)} = \emptyset \tag{26}$$

for any $p_1 \neq p_2$, with p_1 and $p_2 \in \{0, 1, \ldots, N_T - 1\}$, and

$$\bigcup_{p=0}^{N_T-1} \mathcal{S}_m^{(p)} = \mathcal{J} \tag{27}$$

for any m, where $\mathcal{J} \triangleq \{0, 1, \ldots, N-1\}$. It is important to point out that, although our assumption about the use of subcarrier frequencies is strong and entails a reduction by a factor N_T in the transmission rate (with respect to the case in which all the subcarriers are employed by each TX antenna), it paves the way for the development of target detection and estimation algorithms requiring a limited computational effort. In fact, under the last assumption, the sum over p appearing in the RHS of (24) involves a single term different from zero; consequently, (24) becomes

$$R_{m,n}^{(q)} = \frac{s_{m,n}^{(p_a)}}{N} \sum_{k=0}^{K-1} \alpha_k^{(p_a,q)} D_n(f_{D_k})\, v_m(f_{D_k})\, A(R_k) \cdot B^{(p_a,q)}(\theta_k,\phi_k)\, \gamma_n(R_k) + W_n^{(q)}, \tag{28}$$

which represents a sample of the 2D signal employed for channel estimation. Here, p_a denotes the index of the TX antenna to which the nth subcarrier has been assigned in the mth OFDM symbol interval (the dependence of p_a on m and n is not explicitly shown to ease notation). Based on (3), (4), (11)-(13), (15) and (16), it is easy to show that

$$\gamma_n(R_k) D_n(f_{D_k}) = a_n(-F_{\rho_k}), \tag{29}$$

$$v_m(f_{D_k}) = a_m(F_{D_k}) \tag{30}$$

and

$$\alpha_k^{(p_a,q)} A(R_k) B^{(p_a,q)}(\theta_k,\phi_k) = \alpha_k^{(p_a,q)} \exp(j\omega_k)\, a_{p_a}(-F_{H_k})\, a_q(-F_{V_k}), \tag{31}$$

where

$$a_z(F_X) \triangleq \exp(j2\pi z F_X), \tag{32}$$

with $z = p_a$, q, m or n, $X = H_k$, V_k, D_k or ρ_k,

$$F_{H_k} \triangleq d_t \sin(\theta_k)\cos(\phi_k)/\lambda \tag{33}$$

and

$$F_{V_k} \triangleq d_r \sin(\phi_k)/\lambda \tag{34}$$

denote the *normalized horizontal frequency* and the *normalized vertical frequency*, respectively, associated with the kth target,

$$F_{D_k} \triangleq f_{D_k} T_s \tag{35}$$

is the *normalized Doppler frequency*,

$$F_{\rho_k} \triangleq F_{r_k} - F_{D_k} T/(N T_s) \tag{36}$$

is a normalized frequency accounting for both the Doppler of the kth target and its range through the *normalized target delay*[5]

$$F_{r_k} \triangleq 2R_k\, \Delta_f/c \tag{37}$$

and

$$\omega_k \triangleq -2\pi\left(2R_k + \left(x_t^{(0)} + x_r^{(0)}\right)\sin(\theta_k)\cos(\phi_k) + \left(y_t^{(0)} + y_r^{(0)}\right)\sin(\phi_k)\right)/\lambda. \tag{38}$$

Note that:

1) F_{ρ_k} and F_{D_k} satisfy the inequalities $F_{\rho,\min} \leq F_{\rho_k} \leq F_{\rho,\max}$, and $F_{D,\min} \leq F_{D_k} \leq F_{D,\max}$, respectively, with $F_{\rho,\min} = 0$, $F_{\rho,\max} = 1$, $F_{D,\min} = -1/2$ and $F_{D,\max} = 1/2$ for any k;

2) F_{V_k} and F_{H_k} satisfy the inequalities $-d_r/\lambda \leq F_{V_k} \leq d_r/\lambda$ and $-d_r\cos(\phi_k)/\lambda \leq F_{H_k} \leq d_r\cos(\phi_k)/\lambda$, respectively, for any k;

3) the range of F_{H_k} is also limited by the elevation ϕ_k of the kth target for any k (see (33));

4) the ranges of F_{V_k} and F_{H_k} are maximized for $d_r = \lambda/2$ and $d_t = \lambda/2$, respectively.

Based on (29)-(31), eq. (28) can be rewritten as[6]

$$R_{m,n}^{(q)} = s_{m,n}^{(p_a)}\, \hat{H}_{m,n}^{(p_a,q)}, \tag{39}$$

4. The use of *private subcarriers* in JCAS systems has been first proposed in [19] to improve the accuracy of target range and angle estimation through a CS technique.

5. Note that, F_{r_k} is always positive, whereas F_{D_k} is positive (negative) if the kth target is approaching (moving away from) the considered JCAS system.

6. Note that channel symbols $\{s_{m,n}^{(p_a)}\}$ are known to the JCAS receiver for any m, n and p_a.

where[7]

$$\hat{H}_{m,n}^{(p_a,q)} \triangleq \frac{1}{N}\sum_{k=0}^{K-1} A_k\, a_{p_a}\left(-F_{H_k}\right) \cdot a_q\left(-F_{V_k}\right) a_m\left(F_{D_k}\right) a_n\left(-F_{\rho_k}\right) + \bar{W}_{m,n}^{(p_a,q)}, \quad (40)$$

denotes an estimate of the channel frequency response $H_{m,n}^{(p_a,q)}$ characterizing the nth subcarrier frequency in the mth OFDM symbol interval for the VA (p_a, q), $A_k \triangleq \alpha_k \exp(j\omega_k)$ and

$$\bar{W}_{m,n}^{(p_a,q)} \triangleq \frac{W_{m,n}^{(p_a,q)}}{s_{m,n}^{(p_a)}} \quad (41)$$

is the noise sample affecting $\hat{H}_{m,n}^{(p_a,q)}$. The quantity $\hat{H}_{m,n}^{(p_a,q)}$, in (40), represents the noisy measurement produced by the *symbol compensation* block for the VA (p_a, q), the nth subcarrier and the mth OFDM symbol interval (see Fig. 1, where this block is followed by a buffer storing the measurements acquired over each frame). Moreover, the measurements acquired over the OFDM frame and the whole virtual array are collected in the set[8]

$$\mathcal{S}_{\mathbf{H}} \triangleq \left\{\hat{\mathbf{H}}^{(p,q)}; \; p = 0, 1, \ldots, N_T - 1, q = 0, 1, \ldots, N_R - 1\right\}, \quad (42)$$

where $\hat{\mathbf{H}}^{(p,q)} \triangleq [\hat{H}_{m,n}^{(p,q)}]$ represents the $M \times N$ matrix formed by all the measurements acquired through the VA (p, q) over the OFDM frame. Note that this set consists of N_{VA} matrices, one for each of the N_{VA} VAs, and that it represents the output of the last block appearing in Fig. 1.

The measurement model (40) deserves the following comments:

1) The complex gain A_k appearing in its RHS accounts for the phase rotation due to the path delay, the path loss and the gain (attenuation) introduced by the kth target.

2) Since, in all our computer simulations, a $N_s$ary *phase shift keying* (PSK) constellation is adopted for the channel symbols $\{s_{m,n}^{(p_a)}\}$, the 2D sequence of noise samples $\{\bar{W}_{m,n}^{(p_a,q)}\}$ (see (41)) affecting the measurements has the same statistical properties as $\{W_n^{(q)}\}$ (see (28)), i.e., it can be modelled as AWGN (the variance of each sample is denoted $\sigma_{\bar{W}}^2$).

3) The noisy samples $\{\hat{H}_{m,n}^{(p,q)}\}$ of the 4D channel response acquired over a single OFDM frame can be modelled as the superposition of an AWGN process with K 4D complex exponentials, whose amplitude, phase and frequencies provide information about the range, the Doppler and the angular coordinates of the detectable targets. For this reason, target detection and estimation is tantamount to identifying the K complex exponentials that form the useful component of the sequence $\{\hat{H}_{m,n}^{(p,q)}\}$ and to estimating their parameters, respectively.

Finally, it is important to make some considerations about the use of private subcarriers and the criteria that can be adopted in the selection of their subsets $\{\mathcal{S}_m^{(p)}\}$. From the rules illustrated above about the use of private subcarriers it can be easily inferred that the maximum data rate achievable through the proposed transmission scheme is identical to that of a JCAS system equipped with a single TX antenna, i.e., as already mentioned above, it is N_T times lower than that provided by a MIMO system with *shared subcarriers* (e.g., see [19]). In addition, the TX array is not exploited for beamsteering, as suggested, for instance, in [29], where a single-stream beamforming model is assumed. Despite this, the considered JCAS system benefits from the availability of a TX array, since this results in a larger virtual array (i.e., in an increase of the overall number of VAs, N_{VA}) and, consequently, in a better angular resolution [27]. As far as the selection of the subsets $\{\mathcal{S}_m^{(p)}\}$ is concerned, in our computer simulations, a pseudo-random mechanism has been adopted in assigning the N available subcarriers to the N_T TX antennas in the transmission of the mth OFDM symbol of a given frame; moreover, the same pseudo-random pattern has been employed for all the transmitted frames. The choice of this strategy is motivated by the fact that randomly changing the subset of subcarriers from symbol to symbol allows the considered radar system to benefit from *transmit diversity*.

III. DESCRIPTION OF THE PROPOSED APPROACH TO THE ESTIMATION OF MULTIPLE TARGETS

In this section, the problem of developing reduced complexity methods for the detection of multiple targets and for the estimation of their parameters in the MIMO OFDM-based JCAS system described in the previous section is tackled. We first describe a general strategy to devise novel solutions to this problem. Then, we provide some indications about the processing to be accomplished by each of the two main parts it consists of.

A. DESCRIPTION OF THE PROPOSED STRATEGY

Achieving joint ML estimation of an unknown number of targets, given the set of measurements $\mathcal{S}_{\mathbf{H}}$, in (42), is an overly complicated problem, since it involves a large number of parameters to be estimated (more precisely, five parameters per target plus the overall number of targets), even for small values of K. This motivates our interest in the development of sub-optimal methods based on the idea of turning a multidimensional estimation problem into a set of interconnected lower dimensional sub-problems. In the remaining part of this subsection, we illustrate a general strategy, called DRAEC, for the derivation of a new class of such methods. According to this strategy, range and Doppler estimation is decoupled from angular estimation. This explains why its structure, described by the block diagram shown in Fig. 3, contains two *core* blocks, called *range-Doppler estimator* (RDE) and *angular estimator* (AE): in fact, the

7. In the following, the dependence of $\alpha_k^{(p_a,q)}$ on (p_a, q) is neglected; therefore, $\alpha_k = \alpha_k^{(p_a,q)}$ is assumed.

8. In the following, the antenna index p_a is replaced by p (with $p = 0, 1, \ldots, N_T - 1$) for simplicity.

former block accomplishes target detection and jointly estimates target range and Doppler, whereas the second one identifies multiple targets characterized by similar Doppler and ranges, and estimates their azimuth and elevation. Note also that the proposed structure includes a *fusion* block, whose task is merging the information provided by the first two blocks in order to generate a 4D radar image in the form of a point cloud. The processing accomplished by the core blocks can be summarized as follows. Based on the available measurements (i.e., on the set $\mathcal{S}_{\mathbf{H}}$, in (42)), the RDE generates the so-called *target range-Doppler profile* (TRDP), namely a collection of: 1) *range-Doppler* couples at which relevant echoes are detected; 2) an estimate of the complex amplitude associated with each of these couples (the absolute value of such amplitudes allows us to rank the couples on the basis of their perceptual importance). More precisely, the TRDP is represented by the set

$$\mathcal{S}^{(\mathrm{RDE})} \triangleq \left\{\left(\hat{F}_{D_k}, \hat{F}_{r_k}, \hat{A}_k\right);\ k = 0, 1, \ldots, K^{(\mathrm{RDE})} - 1\right\}, \tag{43}$$

where $\hat{F}_{D_k}$, $\hat{F}_{r_k}$ and $\hat{A}_k$ denote the estimates of the normalized Doppler frequency, the normalized delay and the complex amplitude, respectively, associated with the kth range-Doppler bin[9] in which (at least) one target has been detected,[10] and $K^{(\mathrm{RDE})}$ is the overall number of relevant range-Doppler bins identified by the RDE.

The set $\mathcal{S}^{(\mathrm{RDE})}$, in (43), is passed to the AE, which processes it jointly with the set $\mathcal{S}_{\mathbf{H}}$ (see (42)) in order to: 1) identify all the targets associated with each of the range-Doppler-complex amplitude triplets forming the TRDP; 2) generate the so-called *angular profile* (AP), that collects the estimates of the angular parameters and the complex amplitude of all the targets detected within each range-Doppler bin. In practice, the AP information associated with the kth element (i.e., triplet) of $\mathcal{S}^{(\mathrm{RDE})}$ is represented by the set

$$\mathcal{S}_k^{(\mathrm{AE})} \triangleq \left\{\left(\hat{F}_{H_k}[l], \hat{F}_{V_k}[l], \hat{A}_k[l]\right);\ l = 0, 1, \ldots, K_k^{(\mathrm{AE})} - 1\right\}, \tag{44}$$

with $k = 0, 1, \ldots, K^{(\mathrm{RDE})} - 1$; here, $\hat{F}_{H_k}[l]$, $\hat{F}_{V_k}[l]$ and $\hat{A}_k[l]$ denote the estimates of the normalized horizontal frequency, normalized vertical frequency and complex amplitude of the lth target detected in the kth range-Doppler bin, respectively, whereas $K_k^{(\mathrm{AE})}$ represents the overall number of targets detected in that bin. The normalized frequencies $\hat{F}_{H_k}[l]$ and $\hat{F}_{V_k}[l]$ are jointly processed by the fusion block in order to generate, on the basis of (33) and (34), the estimates $\hat{\theta}_k[l]$ and $\hat{\phi}_k[l]$ of the azimuth $\theta_k[l]$ and the elevation $\phi_k[l]$, respectively, characterizing the lth target identified in the kth range-Doppler bin. Moreover, the fusion block processes the estimates $\hat{F}_{D_k}$ and $\hat{F}_{r_k}$ to compute the estimates $\hat{v}_k[l]$ and $\hat{R}_k[l]$ of the velocity $v_k[l]$ and range $R_k[l]$, respectively, on the basis of (9), (35) and (37). Then, the above mentioned estimates are collected in the set

$$\mathcal{S}^{(\mathrm{DRAEC})} \triangleq \bigcup_{k=0}^{K^{(\mathrm{RDE})}-1} \mathcal{S}_k^{(\mathrm{DRAEC})}, \tag{45}$$

where

$$\mathcal{S}_k^{(\mathrm{DRAEC})} \triangleq \left\{\left(\hat{R}_k[l], \hat{v}_k[l], \hat{\theta}_k[l], \hat{\phi}_k[l], \hat{A}_k[l]\right);\ l = 0, 1, \ldots, K_k^{(\mathrm{AE})} - 1\right\}, \tag{46}$$

with $k = 0, 1, .., K^{(\mathrm{RDE})} - 1$. The set $\mathcal{S}^{(\mathrm{DRAEC})}$, in (45), represents the final output of the DRAEC strategy if the RDE is not exploited again. Alternatively, it can be passed to the RDE with the aim of re-estimating the range and Doppler parameters of each of the $K_k^{(\mathrm{AE})}$ detected targets for any k; this step is expected to generate an updated version of the set $\mathcal{S}^{(\mathrm{RDE})}$ (see (43)); fusing this set with the overall AP produces an updated version of the set $\mathcal{S}^{(\mathrm{DRAEC})}$, that collects *finer estimates* of the parameters of all the detected targets.

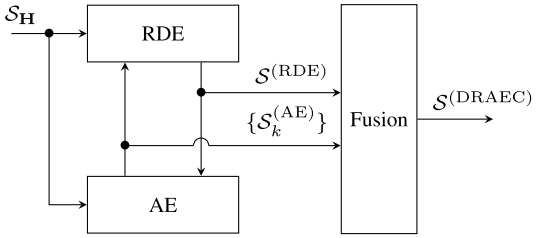

FIGURE 3. Block diagram describing the DRAEC strategy. Two interconnected *core* blocks, namely the RDE and the AE, and a fusion block, generating the final output, are employed.

B. PROCESSING TASKS ACCOMPLISHED BY THE CONSTITUENT BLOCKS

In this subsection, the essential processing tasks accomplished by the RDE and AE blocks appearing in Fig. 3 are sketched; in our description it is assumed, without any loss of generality, that the considered MIMO OFDM-based JCAS system is equipped with the URA illustrated in Fig. 2.

The RDE extracts from the set $\mathcal{S}_{\mathbf{H}}$ (see (42)), collecting N_{VA} matrices, a single matrix, denoted $\hat{\mathbf{H}}^{(p_{\mathrm{R}},q_{\mathrm{R}})}$ and referring to a specific VA (called *reference* VA and associated with the choice $(p, q) = (p_{\mathrm{R}}, q_{\mathrm{R}})$; see Fig. 2). Then, it processes $\hat{\mathbf{H}}^{(p_{\mathrm{R}},q_{\mathrm{R}})}$ to generate the TRDP, i.e., the set $\mathcal{S}^{(\mathrm{RDE})}$, in (43). It is important to point out that:

1) Based on $\hat{\mathbf{H}}^{(p_{\mathrm{R}},q_{\mathrm{R}})}$, the TRDP can be generated by estimating the complex amplitudes and the frequencies of the complex exponentials that form the useful component of the 2D sequence $\{\hat{H}_{m,n}^{(p_{\mathrm{R}},q_{\mathrm{R}})}\}$.

2) The parameter $K^{(\mathrm{RDE})}$ appearing in (43) represents the overall number of range-Doppler bins in which at least a single target is detected. In fact, at this stage, the RDE

9. As shown in the next section, the 2D FFT processing executed by the RDE leads to discretizing the range-Doppler domain and, in particular, to partitioning it into multiple range-Doppler *bins*.

10. Note that the RDE is unable to separate multiple targets whose range and Doppler fall in the same bin.

detects multiple targets, characterized by similar ranges and Dopplers (and, in particular, such that their parameters fall inside in the same range-Doppler bin) as a single target. This explains why, in general, the kth range-Doppler bin selected by the RDE (with $k = 0, 1, \ldots, K^{(\mathrm{RDE})} - 1$) may contain multiple (say, $K_k^{(\mathrm{AE})}$) targets, which are overlapped in the range-Doppler domain, but have distinct angular coordinates.

3) The absolute value of the complex amplitude $\hat{A}_k$ appearing in (43) represents the *perceptual importance* of the kth detected range-Doppler bin (with $k = 0, 1, \ldots, K^{(\mathrm{RDE})}$); in the following, we assume that the elements of $\mathcal{S}^{(\mathrm{RDE})}$ are ordered according to a decreasing perceptual importance, so that $|\hat{A}_{k+1}| \geq |\hat{A}_k|$, with $k = 0, 1, \ldots, K^{(\mathrm{RDE})} - 1$.

The set $\mathcal{S}_{\mathbf{H}}$ and the TRDP (see (42) and (43), respectively) feed the AE, that sequentially accomplishes the three steps listed below.

1) It checks if the kth range-Doppler bin satisfies the inequality

$$|\hat{A}_k|^2 > \mathcal{T}^{(\mathrm{RDE})}, \tag{47}$$

with $k = 0, 1, \ldots, K^{(\mathrm{RDE})}$; here, $\mathcal{T}^{(\mathrm{RDE})}$ is a proper threshold. Any bin not meeting this condition is discarded. This leads to the reduced TRDP

$$\bar{\mathcal{S}}^{(\mathrm{RDE})} \triangleq \left\{ \left(\hat{F}_{D_k}, \hat{F}_{r_k}, \hat{A}_k \right);\ k = 0, 1, \ldots, \bar{K}^{(\mathrm{RDE})} - 1 \right\}, \tag{48}$$

with $\bar{K}^{(\mathrm{RDE})} \leq K^{(\mathrm{RDE})}$.

2) It merges the information provided by the N_{VA} matrices of the set $\mathcal{S}_{\mathbf{H}}$ (see (42)) in $\bar{K}^{(\mathrm{RDE})}$ $N_T \times N_R$ matrices, one for each of $\bar{K}^{(\mathrm{RDE})}$ range-Doppler bins selected in the previous step. The kth matrix (with $k = 0, 1, \ldots, \bar{K}^{(\mathrm{RDE})} - 1$) is denoted $\breve{\mathbf{H}}_k \triangleq [\breve{H}_k^{(p,q)}]$; the element appearing on its pth row and qth column is evaluated as

$$\breve{H}_k^{(p,q)} = \frac{1}{MN} \sum_{m=0}^{M-1} \sum_{n=0}^{N-1} \hat{H}_{m,n}^{(p,q)}\, a_m^*\left(\hat{F}_{D_k}\right) a_n^*\left(-\hat{F}_{\rho_k}\right), \tag{49}$$

with $p = 0, 1, \ldots, N_T - 1$ and with $q = 0, 1, \ldots, N_R - 1$; here, $\hat{F}_{\rho_k}$ represents the estimate of the normalized frequency in (36).

3) It processes the matrix $\breve{\mathbf{H}}_k$ to identify all the targets contained in the kth range-Doppler bin in order to generate the set $\mathcal{S}_k^{(\mathrm{AE})}$ in (44) where, however, $k = 0, 1, \ldots, \bar{K}^{(\mathrm{RDE})} - 1$.

The AE output, i.e., the overall AP, results from merging all the information contained in the $\bar{K}^{(\mathrm{RDE})}$ sets $\{\mathcal{S}_k^{(\mathrm{AE})}\}$ and collects the estimates of all the angular parameters referring to

$$K^{(\mathrm{AE})} \triangleq \sum_{k=0}^{\bar{K}^{(\mathrm{RDE})}-1} K_k^{(\mathrm{AE})} \tag{50}$$

distinct targets. This concludes the AE processing.

It is worth noting that:

1) The term $a_m^*(\hat{F}_{D_k})$ ($a_n^*(-\hat{F}_{\rho_k})$) appearing in the RHS of (49) aims at *compensating* for the factor $a_m(F_{D_k})$ ($a_n(-F_{\rho_k})$) which is visible in the same side of (40); in other words, it is expected to cancel the dependence of $\breve{H}_k^{(p,q)}$ on the Doppler and range of the kth target (leaving, however, the dependence on its *normalized horizontal* and *vertical frequencies*).

2) Similarly as step 1) of the RDE, step 3) of the AE processing requires estimating the complex amplitudes and the frequencies of the overlapped complex exponentials that form the useful component of the 2D sequence $\{\breve{H}_k^{(p,q)}\}$ (with $k = 0, 1, \ldots, \bar{K}^{(\mathrm{RDE})} - 1$).

If the AE output is passed to the RDE, the last block sequentially accomplishes the three steps[11] illustrated below for each of the considered $\bar{K}^{(\mathrm{RDE})}$ range-Doppler bins; in our description of such steps we refer to the kth range-Doppler bin (with $k = 0, 1, \ldots, \bar{K}^{(\mathrm{RDE})} - 1$).

1) The RDE generates the subset

$$\bar{\mathcal{S}}_k^{(\mathrm{AE})} \triangleq \left\{ \left(\hat{F}_{H_k}[l], \hat{F}_{V_k}[l], \hat{A}_k[l] \right);\ l = 0, 1, \ldots, \bar{K}_k^{(\mathrm{AE})} - 1 \right\} \tag{51}$$

of $\mathcal{S}_k^{(\mathrm{AE})}$, in (44), (here, $\bar{K}_k^{(\mathrm{AE})}$ denotes the size of $\bar{\mathcal{S}}_k^{(\mathrm{AE})}$, with $\bar{K}_k^{(\mathrm{AE})} \leq K_k^{(\mathrm{AE})}$); in doing so, it discards the lth element of $\mathcal{S}_k^{(\mathrm{AE})}$ (with $l = 0, 1, \ldots, K_k^{(\mathrm{AE})} - 1$) if

$$|\hat{A}_k[l]|^2 \leq \mathcal{T}^{(\mathrm{AE})}, \tag{52}$$

where $\mathcal{T}^{(\mathrm{AE})}$ is a proper threshold.

2) It merges the information provided by the N_{VA} antennas at the N subcarrier frequencies and over the M OFDM symbol intervals (i.e., over the whole OFDM frame) to generate a set of $\bar{K}_k^{(\mathrm{AE})}$ $M \times N$ matrices, each referring to a single element of the set $\bar{\mathcal{S}}_k^{(\mathrm{AE})}$. More specifically, the matrix associated with the lth element of $\bar{\mathcal{S}}_k^{(\mathrm{AE})}$ (with $l = 0, 1, \ldots, \bar{K}_k^{(\mathrm{AE})} - 1$) is denoted $\breve{\mathbf{H}}_k[l] \triangleq [\breve{H}_{m,n}[k, l]]$; moreover, the element appearing on its mth row and nth column is evaluated as

$$\breve{H}_{m,n}[k, l] \triangleq \frac{1}{N_T N_R} \sum_{p=0}^{N_T-1} \sum_{q=0}^{N_R-1} \hat{H}_{m,n}^{(p,q)} \cdot a_p\left(\hat{F}_{H_k}[l]\right) a_q\left(\hat{F}_{V_k}[l]\right), \tag{53}$$

with $m = 0, 1, \ldots, M - 1$ and $n = 0, 1, \ldots, N - 1$.

3) It processes the matrix $\breve{\mathbf{H}}_k[l]$ (with $l = 0, 1, \ldots, \bar{K}_k^{(\mathrm{AE})} - 1$) in order to estimate the range, Doppler and complex amplitude of the lth target detected in the kth range-Doppler bin. This requires estimating the parameters of a single complex exponential on the basis of the 2D sequence $\{\breve{H}_{m,n}[k, l]\}$ and leads to the *fine* estimates $(\hat{F}_{D_k}[l], \hat{F}_{r_k}[l], \hat{A}_k[l])$ of the normalized Doppler frequency, normalized delay and complex amplitude, respectively, of the above mentioned target. These information are collected in the set

$$\bar{\mathcal{S}}_k^{(\mathrm{RDE})} \triangleq \left\{ \left(\hat{F}_{D_k}[l], \hat{F}_{r_k}[l], \hat{A}_k[l] \right);\ l = 0, 1, \ldots, \bar{K}_k^{(\mathrm{AE})} - 1 \right\}. \tag{54}$$

11. Actually, the first step is ignored if all the targets detected in each range-Doppler bin are taken into consideration.

Note that the term $a_p(\hat{F}_{H_k}[l])$ ($a_q(\hat{F}_{V_k}[l])$) appearing in the RHS of (53) aims at *compensating* for the factor $a_p(-F_{H_k})$ ($a_q(-F_{V_k})$) that appears in the same side of (40); in other words, it is expected to cancel the dependence of $\hat{H}_{m,n}[k,l]$ on the *normalized horizontal* and *vertical frequencies* (i.e., on the angular parameters) of lth target detected in kth range-Doppler bin.

The strategy described above is called *Doppler-range-angle estimation with successive compensation*, or DRAEC, and is summarized in Algorithm 1. Its final output is represented by the set

$$\bar{\mathcal{S}}^{(\mathrm{DRAEC})} \triangleq \bigcup_{k=0}^{\bar{K}^{(\mathrm{RDE})}-1} \bar{\mathcal{S}}_k^{(\mathrm{DRAEC})}. \tag{55}$$

that collects the estimates referring to

$$K^{(\mathrm{DRAEC})} \triangleq \sum_{k=0}^{\bar{K}^{(\mathrm{RDE})}-1} \bar{K}_k^{(\mathrm{AE})} \tag{56}$$

distinct targets; here,

$$\bar{\mathcal{S}}_k^{(\mathrm{DRAEC})} \triangleq \Big\{\Big(\hat{R}_k[l], \hat{v}_k[l], \hat{\theta}_k[l], \hat{\phi}_k[l], \hat{A}_k[l]\Big); \; l = 0, 1, \ldots, \bar{K}_k^{(\mathrm{AE})} - 1\Big\}, \tag{57}$$

represents the contribution due to all the targets detected in the kth range-Doppler bin. Note that, the set $\bar{\mathcal{S}}^{(\mathrm{DRAEC})}$, in (55), results from merging all the information provided the RDE and the AE, namely the sets $\bar{\mathcal{S}}^{(\mathrm{RDE})}$ and $\{\bar{\mathcal{S}}_k^{(\mathrm{AE})}\}$. In other words, the final output is obtained by 1) converting each normalized frequency to the corresponding spatial parameter; 2) associating each target with its set of spatial parameters. These operations are carried out by the fusion block appearing in Fig. 3.

Finally, it is important to stress that the most important task accomplished by both the RDE and the AE is represented by the estimation of the parameters of 2D complex oscillations on the basis of a set of noisy measurements. Different algorithms can be employed for this task; the selection of a specific algorithm leads to a different instance of the DRAEC strategy, as illustrated in the following sections.

IV. DESCRIPTION OF VARIOUS ALGORITHMS FOR THE DETECTION AND THE ESTIMATION OF TWO-DIMENSIONAL COMPLEX OSCILLATIONS

In this section, we concentrate on the problem of detecting multiple overlapped 2D complex exponentials and estimating their parameters in the presence of AWGN. Various estimators, representing distinct solutions to this problem, are illustrated. In all cases, essential mathematical details are provided and a unified mathematical notation is employed. More specifically, it is assumed that: 1) $\{\hat{H}_{m,n}^{(\mathrm{X})}; \; m = 0, 1, \ldots, M-1, \; n = 0, 1, \ldots, N-1\}$ (with X = RDE or X = AE) represents the input sequence[12] of any 2D estimator employed in the RDE or in the AE; 2) the element (m,n) of this sequence can be expressed as

$$\hat{H}_{m,n}^{(\mathrm{X})} \triangleq \sum_{k=0}^{K-1} A_k \, a_m\big(F_{1,k}\big) \, a_n\big(F_{2,k}\big) + W_{m,n}^{(\mathrm{X})}, \tag{58}$$

where $F_{1,k} = F_{D_k}$, $F_{2,k} = -F_{\rho_k}$ ($F_{1,k} = -F_{H_k}$, $F_{2,k} = -F_{V_k}$) if the estimator is employed in the RDE (AE); 3) the parameters A_k, F_{D_k}, F_{ρ_k}, F_{H_k} and F_{V_k} have the same meaning as the corresponding parameters appearing in the RHS of (40) and $W_{m,n}^{(\mathrm{X})}$ is the noise sample affecting $\hat{H}_{m,n}^{(\mathrm{X})}$ (an AWGN model is adopted for the sequence $\{W_{m,n}^{(\mathrm{X})}\}$).

All the algorithms described in the following subsections make use of 2D periodograms. More specifically, *target detection* and *range & Doppler estimation* in the RDE require the computation of the $M_0 \times N_0$ matrix

$$\mathbf{Y}^{(\mathrm{RDE})} = \Big[Y^{(\mathrm{RDE})}[l,p]\Big] \triangleq \mathrm{DSFT}_{M_0,N_0}\Big[\hat{\mathbf{H}}_{\mathrm{ZP}}^{(\mathrm{RDE})}\Big] \triangleq \mathbf{F}_{M_0} \hat{\mathbf{H}}_{\mathrm{ZP}}^{(\mathrm{RDE})} \mathbf{F}_{N_0}^{H}, \tag{59}$$

that represents the order (M_0, N_0) *discrete symplectic Fourier transform* (DSFT) of the $M_0 \times N_0$ matrix

$$\hat{\mathbf{H}}_{\mathrm{ZP}}^{(\mathrm{RDE})} \triangleq \begin{bmatrix} \hat{\mathbf{H}}^{(\mathrm{RDE})} & \mathbf{0}_{M,N_0-N} \\ \mathbf{0}_{M_0-M,N} & \mathbf{0}_{M_0-M,N_0-N} \end{bmatrix}, \tag{60}$$

that results from zero-padding the $M \times N$ matrix $\hat{\mathbf{H}}^{(\mathrm{RDE})} \triangleq [\hat{H}_{m,n}^{(\mathrm{RDE})}]$ (see (58)); here, $\mathbf{F}_N$ represents the order N Fourier matrix (its element (a,b) is equal to ω_N^{ab}/N, where $\omega_N = \exp(-j2\pi/N)$). The element (l,p) of $\mathbf{Y}^{(\mathrm{RDE})}$, in (59), is given by

$$Y^{(\mathrm{RDE})}[l,p] \triangleq \frac{1}{MN} \sum_{m=0}^{M-1} \sum_{n=0}^{N-1} \hat{H}_{m,n}^{(\mathrm{RDE})} \cdot \exp\left(-j2\pi m \frac{l}{M_0}\right) \exp\left(j2\pi n \frac{p}{N_0}\right), \tag{61}$$

where

$$M_0 \triangleq L_1^{(\mathrm{RDE})} M, \tag{62}$$

$$N_0 \triangleq L_2^{(\mathrm{RDE})} N, \tag{63}$$

and $L_1^{(\mathrm{RDE})}$ and $L_2^{(\mathrm{RDE})}$ represent the *oversampling factors* adopted in RDE processing. Note that $Y^{(\mathrm{RDE})}[l,p]$ is associated with the *normalized Doppler frequency*

$$F_D[l] \triangleq l\bar{F}_D - 1/2 \tag{64}$$

and the *normalized frequency* (accounting for both range and Doppler; see (36))

$$F_\rho[p] \triangleq p\bar{F}_\rho, \tag{65}$$

where

$$\bar{F}_D \triangleq 1/M_0 \tag{66}$$

12. This 2D sequence corresponds to $\{\hat{H}_{m,n}^{(p_{\mathrm{R}},q_{\mathrm{R}})}\}$ or $\{\check{H}_{m,n}[k,l]\}$ (see (40) and (53), respectively) in the case of the RDE; it corresponds, instead, to $\{\check{H}_k^{(p,q)}\}$ (see (49)) in the case of the AE.

Algorithm 1: The DRAEC Strategy

Input: The set $\mathcal{S}_{\mathbf{H}}$, in (42), made of N_{VA} $M \times N$ matrices, and the indices of the reference antenna $((p_R, q_R))$.

1 **RDE-1:**

a-Generation of the TRDP: Process $\hat{\mathbf{H}}^{(p_R,q_R)}$ to generate the set $\mathcal{S}^{(\mathrm{RDE})}$ (see (43)), made of $K^{(\mathrm{RDE})}$ elements; one of the estimators described in Section IV is employed in this step.

2 **AE:**

b-Reduction of the TRDP size: Discard some elements of the set $\mathcal{S}^{(\mathrm{RDE})}$ on the basis of their perceptual relevance (see (47)); the resulting set consists of $\bar{K}^{(\mathrm{RDE})}$ elements.

for $k = 0$ *to* $\bar{K}^{(\mathrm{RDE})} - 1$ **do**

c-Doppler and range compensation: Compute the $N_R \times N_T$ matrix $\breve{\mathbf{H}}_k$, whose element (p, q) is defined by (49).

d-Detection and angular estimation of the targets contributing to the kth range-Doppler bin: Detect all the targets contained in the kth range-Doppler bin and estimate their normalized horizontal and vertical frequencies, and their complex amplitude on the basis of the matrix $\breve{\mathbf{H}}_k$ (one of the estimators described in Section IV is employed); this produces the set $\mathcal{S}_k^{(\mathrm{AE})}$, in (44), made of $K_k^{(\mathrm{AE})}$ elements.

3 **RDE-2:**

e-Reduction of the AP size: Discard some elements of the set $\mathcal{S}_k^{(\mathrm{AE})}$, in (44), on the basis of their perceptual relevance (see (52)); the resulting set (see (51)) consists of $\bar{K}_k^{(\mathrm{AE})}$ elements.

for $l = 0$ *to* $\bar{K}_k^{(\mathrm{AE})} - 1$ **do**

f-Angular compensation: Compute the $M \times N$ matrix $\breve{\mathbf{H}}_k[l]$, whose element (m, n) is defined by (53).

g-Fine estimation: Evaluate the fine estimates of the normalized Doppler frequency $F_{D_k}[l]$, the normalized delay $F_{r_k}[l]$, and the complex amplitude $A_k[l]$ of the lth target contained in the kth range-Doppler bin on the basis of the matrix $\breve{\mathbf{H}}_k[l]$; one of the estimators described in Section IV is employed in this step.

end

end

Output: The set $\bar{\mathcal{S}}^{(\mathrm{DRAEC})}$, in (55).

and

$$\bar{F}_\rho \triangleq 1/N_0. \tag{67}$$

Similarly, *angular estimation* in the AE requires the computation of the $\bar{M}_0 \times \bar{N}_0$ matrix

$$\mathbf{Y}^{(\mathrm{AE})} = \left[Y^{(\mathrm{AE})}[l,p]\right] \triangleq \mathrm{IDFT}_{\bar{M}_0,\bar{N}_0}\left[\hat{\mathbf{H}}_{\mathrm{ZP}}^{(\mathrm{AE})}\right] \triangleq \mathbf{F}_{\bar{M}_0}^H \hat{\mathbf{H}}_{\mathrm{ZP}}^{(\mathrm{AE})} \mathbf{F}_{\bar{N}_0}^H, \tag{68}$$

that represents the order $(\bar{M}_0, \bar{N}_0)$ 2D *inverse discrete Fourier transform* (IDFT) of the $\bar{M}_0 \times \bar{N}_0$ matrix $\hat{\mathbf{H}}_{\mathrm{ZP}}^{(\mathrm{AE})}$, that results from zero-padding the $N_T \times N_R$ matrix $\hat{\mathbf{H}}^{(\mathrm{AE})} \triangleq [\hat{H}_{m,n}^{(\mathrm{AE})}]$ (see (58)). In practice, the structure of the matrix $\hat{\mathbf{H}}_{\mathrm{ZP}}^{(\mathrm{AE})}$ is expressed by the RHS of (60) if the matrix $\hat{\mathbf{H}}^{(\mathrm{RDE})}$ and the parameters M, N, M_0 and N_0 are replaced by $\hat{\mathbf{H}}^{(\mathrm{AE})}$ and N_R, N_T, $\bar{M}_0$ and $\bar{N}_0$, respectively; moreover, the element (l, p) of $\mathbf{Y}^{(\mathrm{AE})}$ is given by

$$Y^{(\mathrm{AE})}[l,p] \triangleq \frac{1}{N_R N_T} \sum_{m=0}^{N_R-1} \sum_{n=0}^{N_T-1} \hat{H}_{m,n}^{(\mathrm{AE})} \cdot \exp\left(j2\pi m \frac{l}{\bar{M}_0}\right) \exp\left(j2\pi n \frac{p}{\bar{N}_0}\right), \tag{69}$$

where

$$\bar{M}_0 \triangleq L_1^{(\mathrm{AE})} N_R, \tag{70}$$

$$\bar{N}_0 \triangleq L_2^{(\mathrm{AE})} N_T, \tag{71}$$

and $L_1^{(\mathrm{AE})}$ and $L_2^{(\mathrm{AE})}$ are the *oversampling factors* adopted in AE processing. Furthermore, $Y^{(\mathrm{AE})}[l,p]$ is associated with the *normalized horizontal frequency*

$$F_H[p] \triangleq p\,\bar{F}_H - 1/2 \tag{72}$$

and the *normalized vertical frequency*

$$F_V[l] \triangleq l\,\bar{F}_V - 1/2, \tag{73}$$

where

$$\bar{F}_H \triangleq 1/\bar{N}_0 \tag{74}$$

and

$$\bar{F}_V \triangleq 1/\bar{M}_0. \tag{75}$$

In the remaining part of this section we take into consideration six different estimation algorithms and provide a brief mathematical description of each of them. The first five algorithms are FFT-based methods and, more precisely, are the 2D periodogram method [2], the CSFDEC algorithm derived in [32], the estimation algorithm proposed by Popović-Bugarin and Djukanović in [30], a *modified* version of the estimation algorithm devised by Fan et al. in [33] for solving the problem of channel estimation in a hybrid millimeter-wave massive MIMO system and the *q-shift estimator* (dubbed QSE) developed in [31]. The sixth (and last) algorithm can be considered as an extension to 2D frequency estimation of the algorithm developed by Lee and Chun

in [27]; therefore, it is dubbed *extended Lee algorithm*, or ELA. In the description of each estimation algorithm, we first describe its formulation for the RDE; then, we illustrate the changes required to make its use possible in the AE.

A. TWO-DIMENSIONAL PERIODOGRAM METHOD

This method is based on the idea that the frequencies of the 2D complex exponentials forming the useful component of the sequence $\{\hat{H}^{(\mathrm{X})}_{m,n}\}$ are associated with the peaks of a 2D periodogram. For this reason, if the kth target is considered (with $k = 0, 1, \ldots, \hat{K}-1$, where $\hat{K}$ denotes an estimate of the overall number of targets), the estimates $\hat{F}_{D_k}$ and $\hat{F}_{\rho_k}$ of its normalized frequencies F_{D_k} (35) and F_{ρ_k} (36), respectively, are evaluated as $\hat{F}_{D_k} = F_D[\hat{l}^{(\mathrm{RDE})}_k]$ and $F_{\rho_k} = F_\rho[\hat{p}^{(\mathrm{RDE})}_k]$ (see (64) and (65), respectively), where $(\hat{l}^{(\mathrm{RDE})}_k, \hat{p}^{(\mathrm{RDE})}_k)$ is the value of the couple $(\tilde{l}, \tilde{p})$ associated with the kth of the $\hat{K}$ most relevant local maxima (peaks) of the 2D sequence $\{|Y^{(\mathrm{RDE})}[\tilde{l}, \tilde{p}]|^2;\ \tilde{l} \in \mathcal{S}_{M_0},\ \tilde{p} \in \mathcal{S}_{N_0}\}$, $Y^{(\mathrm{RDE})}[l, p]$ is expressed by (61) and

$$\mathcal{S}_U \triangleq \{0, 1, \ldots, U-1\} \tag{76}$$

for any positive integer U.

This algorithm can be also used in the AE block to evaluate the estimates $\hat{F}_{H_k} = F_H[\hat{p}^{(\mathrm{AE})}_k]$ and $\hat{F}_{V_k} = F_V[\hat{l}^{(\mathrm{AE})}_k]$ (see (72) and (73), respectively) of the normalized frequencies F_{H_k} (33) and F_{V_k} (34); the couple of $(\hat{l}^{(\mathrm{AE})}_k, \hat{p}^{(\mathrm{AE})}_k)$ is generated in a similar way as $(\hat{l}^{(\mathrm{RDE})}_k, \hat{p}^{(\mathrm{RDE})}_k)$, the only difference being represented by the fact that $Y^{(\mathrm{RDE})}[l, p]$, in (61), is replaced by $Y^{(\mathrm{AE})}[l, p]$, in (69).

The estimation accuracy of this method can be improved by:

1) Extracting an $I_l \times I_p$ sub-matrix (where I_l and I_p denote the interpolation orders adopted in the Doppler and range domains, respectively), whose central element is $Y^{(\mathrm{X})}[\hat{l}^{(\mathrm{X})}_k, \hat{p}^{(\mathrm{X})}_k]$ (with $k = 0, 1, \ldots, \hat{K}-1$ and X = RDE or AE) from $\mathbf{Y}^{(\mathrm{X})}$ in order to generate a more detailed representation of the analyzed spectrum through the *interpolation*[13] of the sub-matrix elements.

2) Identifying the peak of the interpolated spectrum over the considered 2D domain.

B. COMPLEX SINGLE FREQUENCY DELAY ESTIMATION AND CANCELLATION ALGORITHM

The second FTT-based method combines a single 2D tone estimator, named *complex single frequency delay estimator* (CSFDE), with a serial cancellation procedure. This algorithm can be exploited by the RDE block as it is, whereas some modifications are required if it is employed in the AE block. For this reason, we first focus on its use in the RDE and, then, we illustrate the changes to be made for its use in the AE.

13. In our computer simulations, the 'spline' interpolation (*interp2* function) of MATLAB R2022b has been employed.

The derivation of the CSFDE is based on the assumptions that: 1) $K = 1$ in the model (58) for $\hat{H}^{(\mathrm{RDE})}_{m,n}$; 2) the unknown frequencies $F_{1,0} = F_D$ and $F_{2,0} = -F_\rho$ appearing in that model can be represented as $F_D = F_{D,c} + \delta_D \bar{F}_D$ and $F_\rho = F_{\rho,c} + \delta_\rho \bar{F}_\rho$, respectively, where $F_{D,c}$ ($F_{\rho,c}$) is a *coarse estimate* of F_D (F_ρ), δ_D (δ_ρ) is the associated *residual*, and $\bar{F}_D$ ($\bar{F}_\rho$) is expressed by (66) (67) and represents the normalized fundamental frequency characterizing an order M_0 FFT (N_0 IFFT).

The CSFDE first exploits the 2D periodogram method to detect a single tone and to compute a coarse estimate of its complex amplitude A and frequencies; then, it makes use of an iterative procedure for estimating the residuals and refining the complex amplitude. More specifically, in the *initialization* of the CSFDE, the following quantities are computed:

1) The set of 13 $M_0 \times N_0$ matrices $\{\bar{\mathbf{Y}}_{k_1,k_2} = [\bar{Y}_{k_1,k_2}[l, p]]\}$, with $k_1,\ k_2 = 0, 1, 2, 3$, and $(k_1, k_2) \neq (0, 3),\ (3, 0)$ and $(3, 3)$; here,

$$\bar{\mathbf{Y}}_{k_1,k_2} \triangleq \mathrm{DSFT}_{M_0,N_0}\left[\hat{\mathbf{H}}^{(k_1,k_2)}_{\mathrm{ZP}}\right] \tag{77}$$

is the order (M_0, N_0) DSFT (see (59)) of the matrix $\hat{\mathbf{H}}^{(k_1,k_2)}_{\mathrm{ZP}}$ that results from zero padding[14] the $M \times N$ matrix $\hat{\mathbf{H}}^{(k_1,k_2)} \triangleq [\hat{H}^{(k_1,k_2)}_{m,n}]$ and

$$\hat{H}^{(k_1,k_2)}_{m,n} \triangleq m^{k_1} n^{k_2} \hat{H}^{(\mathrm{RDE})}_{m,n}, \tag{78}$$

with $m = 0, 1, \ldots, M-1$ and $n = 0, 1, \ldots, N-1$.

2) The coarse estimates $\hat{F}^{(0)}_{D,c} = F_D[\hat{l}^{(0)}]$ and $\hat{F}^{(0)}_{\rho,c} = F_\rho[\hat{p}^{(0)}]$ of F_D and F_ρ, respectively (see (64) and (65), respectively), where

$$\left(\hat{l}^{(0)}, \hat{p}^{(0)}\right) = \arg \max_{\tilde{l} \in \mathcal{S}_{M_0}, \tilde{p} \in \mathcal{S}_{N_0}} \left|\bar{Y}_{0,0}\left[\tilde{l}, \tilde{p}\right]\right|^2. \tag{79}$$

3) The initial estimate

$$\hat{A}^{(0)} = \bar{Y}_{0,0}\left(\hat{F}^{(0)}_{D,c}, \hat{F}^{(0)}_{\rho,c}\right) \tag{80}$$

of the complex amplitude A; here,[15]

$$\bar{Y}_{k_1,k_2}\left(\tilde{F}_D, \tilde{F}_\rho\right) \triangleq \frac{1}{MN} \sum_{m=0}^{M-1} \sum_{n=0}^{N-1} \hat{H}^{(k_1,k_2)}_{m,n} \cdot \exp\left(j2\pi n \tilde{F}_\rho\right) \exp\left(-j2\pi m \tilde{F}_D\right). \tag{81}$$

4) The coefficients

$$\begin{aligned} &b_\Omega\left(F_D, F_\rho\right) \\ &= \hat{\Delta}^3\, \Im\left\{\hat{A}^* \bar{Y}_{2,3}\left(F_D, F_\rho\right)\right\}/3 - \hat{\Delta}^2\, \Re\left\{\hat{A}^* \bar{Y}_{2,2}\left(F_D, F_\rho\right)\right\} \\ &\quad - 2\hat{\Delta}\, \Im\left\{\hat{A}^* \bar{Y}_{2,1}\left(F_D, F_\rho\right)\right\} + 2\Re\left\{\hat{A}^* \bar{Y}_{2,0}\left(F_D, F_\rho\right)\right\}, \end{aligned} \tag{82}$$

14. In practice, the structure of the matrix $\hat{\mathbf{H}}^{(k_1,k_2)}_{\mathrm{ZP}}$ is the same as that of $\hat{\mathbf{H}}^{(\mathrm{RDE})}_{\mathrm{ZP}}$ (60); the only difference between them is due to the fact that the matrix $\hat{\mathbf{H}}^{(\mathrm{RDE})}$ appearing in the definition of the former matrix is replaced by $\hat{\mathbf{H}}^{(k_1,k_2)}$ in that of the latter one. For this reason, the parameters M_0 and N_0 are still expressed by (62) and (63), respectively.

15. Note that: a) $\hat{H}^{(0,0)}_{m,n} = \hat{H}^{(\mathrm{RDE})}_{m,n}$ (see (78)); b) $\bar{Y}_{k_1,k_2}(\tilde{F}_D, \tilde{F}_\rho) = \bar{Y}_{k_1,k_2}[\tilde{l}, \tilde{p}]$ if $\tilde{F}_D = F_D[\tilde{l}]$ and $\tilde{F}_\rho = F_\rho[\tilde{p}]$ for any integer $\tilde{l}$ and $\tilde{p}$.

$$c_{\Omega}(F_D, F_\rho) = \hat{\Delta}^3\,\Re\{\hat{A}^*\bar{Y}_{1,3}(F_D, F_\rho)\}/3 + \hat{\Delta}^2\,\Im\{\hat{A}^*\bar{Y}_{1,2}(F_D, F_\rho)\} - 2\hat{\Delta}\,\Re\{\hat{A}^*\bar{Y}_{1,1}(F_D, F_\rho)\} - 2\Im\{\hat{A}^*\bar{Y}_{1,0}(F_D, F_\rho)\}, \quad (83)$$

$$b_{\Delta}(F_D, F_\rho) = -\hat{\Omega}^3\,\Im\{\hat{A}^*\bar{Y}_{3,2}(F_D, F_\rho)\}/3 - \hat{\Omega}^2\,\Re\{\hat{A}^*\bar{Y}_{2,2}(F_D, F_\rho)\} + 2\hat{\Omega}\,\Im\{\hat{A}^*\bar{Y}_{1,2}(F_D, F_\rho)\} + 2\Re\{\hat{A}^*\bar{Y}_{0,2}(F_D, F_\rho)\} \quad (84)$$

and

$$c_{\Delta}(F_D, F_\rho) = \hat{\Omega}^3\,\Re\{\hat{A}^*\bar{Y}_{3,1}(F_D, F_\rho)\}/3 - \hat{\Omega}^2\,\Im\{\hat{A}^*\bar{Y}_{2,1}(F_D, F_\rho)\} - 2\hat{\Omega}\,\Re\{\hat{A}^*\bar{Y}_{1,1}(F_D, F_\rho)\} + 2\Im\{\hat{A}^*\bar{Y}_{0,1}(F_D, F_\rho)\}, \quad (85)$$

under the assumption that $(F_D, F_\rho) = (F_D[\hat{l}^{(0)}], F_\rho[\hat{p}^{(0)}])$ (so that $\bar{Y}_{k_1,k_2}(F_D, F_\rho) = \bar{Y}_{k_1,k_2}[\hat{l}^{(0)}, \hat{p}^{(0)}]$).

5) The initial estimates $\hat{\Omega}^{(0)}$ and $\hat{\Delta}^{(0)}$ of $\Omega \triangleq 2\pi\delta_D$ and $\Delta \triangleq 2\pi\delta_\rho$ as

$$\hat{X}^{(0)} = -c_X/b_X, \quad (86)$$

with $X = \Omega$ and $X = \Delta$, respectively.

6) The initial fine estimates

$$\hat{F}_D^{(0)} = \hat{F}_{D,c}^{(0)} + \hat{\Omega}^{(0)}/(2\pi) \quad (87)$$

and

$$\hat{F}_\rho^{(0)} = \hat{F}_{\rho,c}^{(0)} + \hat{\Delta}^{(0)}/(2\pi) \quad (88)$$

of F_D and F_ρ, respectively. This concludes the initialization, which is followed by an iterative procedure whose index i is set to 1. The ith iteration of this procedure is fed by the estimates $\hat{F}_D^{(i-1)}$, $\hat{F}_\rho^{(i-1)}$ and $\hat{A}^{(i-1)}$ of F_D, F_ρ and A, respectively, and produces the new estimates $\hat{F}_D^{(i)}$, $\hat{F}_\rho^{(i)}$ and $\hat{A}^{(i)}$ of the same quantities (with $i = 1, 2, \ldots, N_{\rm it}$, where $N_{\rm it}$ is the overall number of iterations to be selected at the beginning of the algorithm). The procedure adopted for the evaluation of $\hat{F}_D^{(i)}$, $\hat{F}_\rho^{(i)}$ and $\hat{A}^{(i)}$ consists of the two steps described below.

1) *Estimation of the normalized Doppler and the normalized delay* - The new estimates $\hat{\Omega}^{(i)}$ and $\hat{\Delta}^{(i)}$ of Ω and Δ, respectively, are computed on the basis of (86); in the evaluation of the coefficients c_X and b_X appearing in that equation (with $X = \Omega$ and Δ), $\hat{A} = \hat{A}^{(i-1)}$ and $(F_D, F_\rho) = (\hat{F}_D^{(i-1)}, \hat{F}_\rho^{(i-1)})$ are assumed. Then,

$$\hat{F}_D^{(i)} = \hat{F}_D^{(i-1)} + \hat{\Omega}^{(i)}/(2\pi) \quad (89)$$

and

$$\hat{F}_\rho^{(i)} = \hat{F}_\rho^{(i-1)} + \hat{\Delta}^{(i)}/(2\pi) \quad (90)$$

are computed.

It is worth mentioning that an alternative to (81) for the evaluation of $\bar{Y}_{k_1,k_2}(\tilde{F}_D, \tilde{F}_\rho)$ in (82)–(85) is represented by the use of a 2D interpolation method applied to a $I_l \times I_p$ submatrix[16] of $\bar{\mathbf{Y}}_{k_1,k_2}$ (77); the need of interpolation originates from the fact that, in general, $\hat{F}_D^{(i-1)}$ and $\hat{F}_\rho^{(i-1)}$ cannot be expressed as $F_D[l]$ and $F_\rho[p]$, respectively, with a proper choice of the integers l and p (see (64) and (65), respectively).

2) *Estimation of the complex amplitude* - The new estimate $\hat{A}^{(i)}$ of $\hat{A}$ is evaluated by means of (80); in doing so, the couple $(\hat{F}_D^{(i)}, \hat{F}_\rho^{(i)})$ is used in place of $(\hat{F}_{D,c}^{(0)}, \hat{F}_{\rho,c}^{(0)})$.

After that the last step has been carried out, the index i is incremented by one and a new iteration is started. At the end of the last (i.e., of the $N_{\rm it}$th) iteration, the fine estimates $\hat{F}_D = \hat{F}_D^{(N_{\rm it})}$, $\hat{F}_\rho = \hat{F}_\rho^{(N_{\rm it})}$ and $\hat{A} = \hat{A}^{(N_{\rm it})}$ of F_D, F_ρ and A, respectively, become available and the algorithm stops.

The CSFDE algorithm represents the core of the CSFDEC algorithm, which is used to recursively estimate the multiple tones forming the useful component of the complex sequence $\{\hat{H}_{m,n}^{(\rm RDE)}\}$, whose (m, n)th element is expressed by (58) with $K \geq 1$ and, in general, *unknown*. The CSFDEC algorithm is initialized by:

1) Running the CSFDE algorithm to compute the initial estimates $\hat{F}_{D_0}^{(0)}$, $\hat{F}_{\rho_0}^{(0)}$ and $\hat{A}_0^{(0)}$ of the parameters F_{D_0}, F_{ρ_0} and A_0, respectively, that characterize the first target.

2) Setting the recursion index i to 1 and $\bar{\mathbf{Y}}_{0,0}^{(0)} = \bar{\mathbf{Y}}_{0,0}$ (see (77) with $k_1 = k_2 = 0$).

Then, a recursive procedure is started. The ith recursion of this procedure is fed by the vectors $\hat{\mathbf{F}}_D^{(i-1)} = [\hat{F}_{D_0}^{(i-1)}, \hat{F}_{D_1}^{(i-1)}, , \ldots, \hat{F}_{D_{i-1}}^{(i-1)}]^T$, $\hat{\mathbf{F}}_\rho^{(i-1)} = [\hat{F}_{\rho_0}^{(i-1)}, \hat{F}_{\rho_1}^{(i-1)}, \cdots, \hat{F}_{\rho_{i-1}}^{(i-1)}]^T$ and $\hat{\mathbf{A}}^{(i-1)} = [\hat{A}_0^{(i-1)}, \hat{A}_1^{(i-1)}, \cdots, \hat{A}_{i-1}^{(i-1)}]^T$, collecting the estimates of the normalized Doppler frequency, normalized delay and complex amplitude, respectively, of the i tones detected and estimated in the previous recursions, and generates the new vectors $\hat{\mathbf{F}}_D^{(i)}$, $\hat{\mathbf{F}}_\rho^{(i)}$ and $\hat{\mathbf{A}}^{(i)}$ after: 1) estimating the parameters $\hat{F}_{D_i}^{(i)}$, $\hat{F}_{\rho_i}^{(i)}$ and $\hat{A}_i^{(i)}$ of the new (i.e., of the ith) tone (if any); 2) refining the estimates of the i tones available at the beginning of the considered recursion. The procedure employed for accomplishing all this consists of three steps and can be summarized as follows (further details can be found in [32, Sec. III-B]).

1) The *residual spectrum* $\bar{\mathbf{Y}}_{0,0}^{(i)}$ is computed by subtracting from $\bar{\mathbf{Y}}_{0,0}^{(i-1)}$the contribution given by the ith estimated 2D tone. Then, if the overall energy $\varepsilon_{0,0}[i] \triangleq \|\bar{\mathbf{Y}}_{0,0}^{(i)}\|^2$ of the vector $\bar{\mathbf{Y}}_{0,0}^{(i)}$ satisfies the inequality $\varepsilon_{0,0}[i] < \mathcal{T}^{(\rm CSFDEC)}$ (where $\mathcal{T}^{(\rm CSFDEC)}$ is a proper threshold), the algorithm stops after executing step 3) (see below) and the estimate $\hat{K} = i$ of K is generated;[17] otherwise, a new tone is detected and a preliminary estimate of its parameters is obtained. Note that, in the last case, the *residual spectra* $\{\bar{\mathbf{Y}}_{k_1,k_2}^{(i)}\}$ (with $k_1, k_2 = 0, 1, 2, 3$, and $(k_1, k_2) \neq (0, 0), (0, 3), (3, 0)$ and $(3, 3)$) are computed by subtracting from each matrix of the set $\{\bar{\mathbf{Y}}_{k_1,k_2}^{(i-1)}\}$ the contribution given to it by the ith estimated 2D tone.

2) Multiple (say, $\bar{N}_{\rm it}$) iterations are executed to *refine* the estimate of the parameters of the new tone detected

16. In the following, I_M and I_N denote the *interpolation orders* adopted for the first and second dimension, respectively, of that matrix.

17. If K is known, the computation of the energy $\varepsilon_{0,0}[i]$ and its comparison with a threshold are not required; in fact, in this case, the CSFDEC algorithm stops at the end of its Kth recursion.

in the previous step. The processing accomplished in this step follows closely that described in the refinement part (i.e., in the second step) of the CSFDE. For this reason, in each iteration, a new estimate of the complex amplitude and of the two residuals of the ith tone are computed.

3) Each of the i detected tones is *re-estimated* after cancelling the leakage due to all the other $(i-1)$ tones. This allows to progressively refine the amplitude, normalized Doppler frequency and normalized delay of each tone, thus generating the final estimates. Note that, in principle, this re-estimation procedure can be repeated multiple (say, N_{REF}) times.

As already mentioned above, the CSFDEC algorithm can also be employed in the AE. However, this requires:

1) Using $\hat{H}_{m,n}^{(\mathrm{AE})}$ (see (58)) in place of $\hat{H}_{m,n}^{(\mathrm{RDE})}$ in the evaluation of $\hat{H}_{m,n}^{(k_1,k_2)}$ according to (78).

2) Evaluating the initial estimate of the complex amplitude of the strongest 2D tone as (see (80))

$$\hat{A}^{(0)} = \bar{Y}_{0,0}\Big(\hat{F}_{V,c}^{(0)}, \hat{F}_{H,c}^{(0)}\Big), \tag{91}$$

where $\hat{F}_{V,c}^{(0)} = F_V[\hat{l}_k^{(0)}]$ and $\hat{F}_{H,c}^{(0)} = F_H[\hat{p}_k^{(0)}]$ (see (72) and (73), respectively) are the coarse estimates of the normalized vertical and horizontal frequencies, respectively.

3) Replacing (84) and (85) with

$$\begin{aligned} &b_{\Delta}(F_V, F_H) \\ &= -\hat{\Omega}^3\, \Im\big\{\hat{A}^* \bar{Y}_{3,2}(F_V, F_H)\big\}/3 + \hat{\Omega}^2\, \Re\big\{\hat{A}^* \bar{Y}_{2,2}(F_V, F_H)\big\} \\ &\quad + 2\hat{\Omega}\, \Im\big\{\hat{A}^* \bar{Y}_{1,2}(F_V, F_H)\big\} - 2\Re\{\hat{A}^* \bar{Y}_{0,2}(F_V, F_H)\} \end{aligned} \tag{92}$$

and

$$\begin{aligned} &c_{\Delta}(F_V, F_H) \\ &= \hat{\Omega}^3\, \Re\big\{\hat{A}^* \bar{Y}_{3,1}(F_V, F_H)\big\}/3 + \hat{\Omega}^2\, \Im\big\{\hat{A}^* \bar{Y}_{2,1}(F_V, F_H)\big\} \\ &\quad - 2\hat{\Omega}\, \Re\big\{\hat{A}^* \bar{Y}_{1,1}(F_V, F_H)\big\} - 2\Im\big\{\hat{A}^* \bar{Y}_{0,1}(F_V, F_H)\big\}, \end{aligned} \tag{93}$$

respectively.

The CSFDEC algorithm is summarized in Algorithm 2 for the case in which K is unknown. If K is known, in step d) of the frequency estimation procedure, the evaluation of the energy $\varepsilon_{0,0}[i]$ and its comparison with a threshold are replaced by a comparison of the iteration index i with K; if $i = K$, step e) is executed, otherwise i is increased by one and the algorithm proceeds with step b).

Algorithm 2: CSFDEC Algorithm

Input: The matrices $\{\hat{\mathbf{H}}_{\mathrm{ZP}}^{(k_1,k_2)}; k_1, k_2 = 0, 1, 2 \text{ and } 3\}$, the overall number of iterations of the CSFDE (N_{it}), the overall number of iterations in the initialization and re-estimation phases ($\bar{N}_{\mathrm{it}}$), the overall number of re-estimation steps (N_{REF}) and the detection threshold ($\mathcal{T}^{(\mathrm{CSFDEC})}$).

1 **Initialization:**
a-Compute the matrices $\{\bar{\mathbf{Y}}_{k_1,k_2}; k_1, k_2 = 0, 1, 2, 3\}$ (see (77)) and set $\bar{\mathbf{Y}}_{k_1,k_2}^{(0)} = \bar{\mathbf{Y}}_{k_1,k_2}$, with $(k_1, k_2) \neq (0, 3)$, $(3, 0)$ and $(3, 3)$. Then, set the recursion index i to one and the re-estimation index r to one.

2 **Frequency estimation:**
b-Run the CSFDE algorithm to compute the estimates $\hat{F}_{D_i}^{(i)}$, $\hat{F}_{\rho_i}^{(i)}$ ($\hat{F}_{V_i}^{(i)}$, $\hat{F}_{H_i}^{(i)}$) and $\hat{A}_i^{(i)}$ on the basis of (82)–(86) ((82), (83), (86), (92) and (93)) for the RDE (AE).
c-Compute the residual spectra $\{\bar{\mathbf{Y}}_{k_1,k_2}^{(i)}; k_1, k_2 = 0, 1, 2, 3\}$, with $(k_1, k_2) \neq (0, 3)$, $(3, 0)$ and $(3, 3)$ (see [32], [Sec. III-B, eqs. (53) and (55)]).
d-Compute the energy $\varepsilon_{0,0}[i] \triangleq \|\bar{\mathbf{Y}}_{0,0}^{(i)}\|^2$; then, if $\varepsilon_{0,0}[i] < \mathcal{T}^{(\mathrm{CSFDEC})}$, go to step **e**); otherwise increase the recursion index i by one and go to step **b**).
e-If $r = N_{\mathrm{REF}}$, go to **Output**; otherwise, increase the re-estimation index r by one and go to **f**).

3 **Re-estimation cycle:**
f-set $\bar{\mathbf{Y}}_{k_1,k_2}^{(0)} = \bar{\mathbf{Y}}_{k_1,k_2}$ for $k_1, k_2 = 0, 1, 2, 3$ (with $(k_1, k_2) \neq (0, 3)$, $(3, 0)$ and $(3, 3)$); then, set the recursion index i to one and go to **b**).

4 **Output:** 1) The estimates $\hat{\mathbf{F}}_D^{(i)}$, $\hat{\mathbf{F}}_\rho^{(i)}$ ($\hat{\mathbf{F}}_V^{(i)}$, $\hat{\mathbf{F}}_H^{(i)}$) and $\hat{\mathbf{A}}^{(i)}$ if the RDE (AE) is considered; 2) the estimate $\hat{K} = i$ of K.

C. POPOVIĆ ALGORITHM

The third FFT-based method (namely, Alg-P) computes the frequency estimates through a serial refinement and cancellation procedure based on the computation of a set of shifted DFT coefficients and their subsequent parabolic fitting. If employed in the RDE, it is fed by the complex sequence $\{\hat{H}_{m,n}^{(\mathrm{RDE})}\}$ and it is initialized by setting the target index k to zero and $H_{m,n}^{(0)} = \hat{H}_{m,n}^{(\mathrm{RDE})}$ for $m = 0, 1, \ldots, M-1$ and $n = 0, 1, \ldots, N-1$. Then, it sequentially executes the three steps described below for the kth target (with $k = 0, 1, \ldots, \hat{K}-1$, where $\hat{K}$ is an estimate of K).

1) *2D periodogram maximization* - In this step, the coarse estimates of the normalized Doppler frequency F_{D_k} and the normalized range frequency F_{ρ_k} are evaluated as $\hat{F}_{D,c}^{(k)} = F_D[\hat{l}_k^{(0)}]$ and $\hat{F}_{\rho,c}^{(k)} = F_\rho[\hat{p}_k^{(0)}]$, respectively (see (64) and (65), respectively); here,

$$\Big(\hat{l}_k^{(0)}, \hat{p}_k^{(0)}\Big) = \underset{\tilde{l} \in \mathcal{S}_{M_0}, \tilde{p} \in \mathcal{S}_{N_0}}{\arg\max} \Big|Y^{(k)}[\tilde{l}, \tilde{p}]\Big|^2, \tag{94}$$

and $Y^{(k)}[l, p]$ is defined in a similar way as $Y^{(\mathrm{RDE})}[l, p]$, in (61), the only difference being represented by the fact that $\hat{H}_{m,n}^{(\mathrm{RDE})}$ is replaced by $H_{m,n}^{(k)}$ (the evaluation of $H_{m,n}^{(k)}$ is illustrated below).

2) *Frequency refinement and amplitude estimation* - In this step, the fine estimates $\hat{F}_{D_k}$ and $\hat{F}_{\rho_k}$ of F_{D_k} and F_{ρ_k}, respectively, are computed according to the formula (see [30, Table 1, eqs. (10)–(11)])

$$\hat{F}_X = \frac{1}{2}\frac{\Gamma_{\mathrm{NUM}}}{\Gamma_{\mathrm{DEN}}}, \tag{95}$$

with $X = D$ or ρ; here,

$$\begin{aligned}\Gamma_{\mathrm{NUM}} = {} & \psi_{X,3}^2\big(P_{X,1} - P_{X,2}\big) + \psi_{X,2}^2\big(P_{X,3} - P_{X,1}\big) \\ & + \psi_{X,1}^2\big(P_{X,2} - P_{X,3}\big),\end{aligned} \tag{96}$$

$$\begin{aligned}\Gamma_{\mathrm{DEN}} = {} & \psi_{X,3}\big(P_{X,1} - P_{X,2}\big) + \psi_{X,2}\big(P_{X,3} - P_{X,1}\big) \\ & + \psi_{X,1}\big(P_{X,2} - P_{X,3}\big),\end{aligned} \tag{97}$$

$\psi_{X,i} \triangleq \delta_{X,c} + (i-2)/(2\,Q_0)$ (with $i = 1, 2$ and 3), $Q = M$ ($Q = N$) if $X = D$ (if $X = \rho$),

$$\delta_{D,c} \triangleq \hat{F}_{D,c} + \frac{1}{\pi}\arctan(\tan(\pi/M_0)\Re\{\Theta_D\}), \tag{98}$$

$$\delta_{\rho,c} \triangleq \hat{F}_{\rho,c} + \frac{1}{\pi}\arctan\big(\tan(\pi/N_0)\Re\big\{\Theta_\rho\big\}\big), \tag{99}$$

$$\Theta_D \triangleq \frac{Y^{(k)}\big(\hat{l}-1,\hat{p}\big) - Y^{(k)}\big(\hat{l}+1,\hat{p}\big)}{2Y^{(k)}\big(\hat{l},\hat{p}\big) - Y^{(k)}\big(\hat{l}-1,\hat{p}\big) - Y^{(k)}\big(\hat{l}+1,\hat{p}\big)}, \tag{100}$$

$$\Theta_\rho \triangleq \frac{Y^{(k)}\big(\hat{l},\hat{p}-1\big) - Y^{(k)}\big(\hat{l},\hat{p}+1\big)}{2Y^{(k)}\big(\hat{l},\hat{p}\big) - Y^{(k)}\big(\hat{l},\hat{p}-1\big) - Y^{(k)}\big(\hat{l},\hat{p}+1\big)}, \tag{101}$$

$$P_{D,i} \triangleq \left|\sum_{m=0}^{M-1}\sum_{n=0}^{N-1}\hat{H}_{m,n}^{(\mathrm{RDE})}\exp\big(-j2\pi\big(m\,\psi_{D,i} - n\,\psi_{r,2}\big)\big)\right| \tag{102}$$

and

$$P_{\rho,i} \triangleq \left|\sum_{m=0}^{M-1}\sum_{n=0}^{N-1}\hat{H}_{m,n}^{(\mathrm{RDE})}\exp\big(-j2\pi\big(m\,\psi_{D,2} - n\,\psi_{\rho,i}\big)\big)\right|, \tag{103}$$

with $i = 1, 2$ and 3. Finally, an estimate of the complex amplitude A_k is evaluated on the basis of (80), where $(\hat{F}_{D,c}^{(0)}, \hat{F}_{\rho,c}^{(0)})$ is replaced by $(\hat{F}_{D_k}, \hat{F}_{\rho_k})$.

3) *Target cancellation* - In this step, the contribution of the $(k+1)$ previously detected targets is subtracted from $\{\hat{H}_{m,n}^{(\mathrm{RDE})}\}$; this produces the 2D residual sequence $\{H_{m,n}^{(k+1)}\}$, where

$$H_{m,n}^{(k+1)} \triangleq \hat{H}_{m,n}^{(\mathrm{RDE})} - \sum_{i=0}^{k}\hat{A}_i\,a_m\big(\hat{F}_{D_i}\big)a_n\big(-\hat{F}_{\rho_i}\big), \tag{104}$$

with $m = 0, 1, \ldots, M-1$ and $n = 0, 1, \ldots, N-1$. Then, the residual spectrum $\mathbf{Y}^{(k+1)} \triangleq [Y^{(k+1)}[l,p]]$ is computed; the expression of the element (l,p) of this $M_0 \times N_0$ matrix is obtained from that of $Y^{(\mathrm{RDE})}[l,p]$, in (61), by simply replacing $\hat{H}_{m,n}^{(\mathrm{RDE})}$ with $H_{m,n}^{(k+1)}$ (additional details can be found in the description of the *sinousoid removal* step available in [30, Table 2, eq. (12)–(13)]). If the energy $\varepsilon[k+1] \triangleq \|\mathbf{Y}^{(k+1)}\|^2$ is smaller than $\mathcal{T}^{(P)}$, where $\mathcal{T}^{(P)}$ is a proper threshold, the algorithm stops and the estimate $\hat{K} = k+1$ of K is generated; otherwise, k is increased by one and the three steps described above are accomplished again.

The use of Alg-P in the AE requires the following modifications: 1) the spectral coefficient $Y^{(k)}[\tilde{l},\tilde{p}]$ appearing in the RHS of (94) is still expressed by (69), where, however, $\hat{H}_{m,n}^{(\mathrm{AE})}$ is replaced by

$$H_{m,n}^{(k+1)} \triangleq \hat{H}_{m,n}^{(\mathrm{AE})} - \sum_{i=0}^{k}\hat{A}_i\,a_m\big(-\hat{F}_{V_i}\big)a_n\big(-\hat{F}_{H_i}\big); \tag{105}$$

2) formula (95) (with $X = V$ or H) is employed to compute the estimates $\hat{F}_{H_k}$ and $\hat{F}_{V_k}$ of F_{H_k} and F_{V_k}, but the quantities

$$P_{H,i} \triangleq \left|\sum_{m=0}^{M-1}\sum_{n=0}^{N-1}\hat{H}_{m,n}^{(\mathrm{AE})}\exp\big(j2\pi\big(m\,\psi_{V,2} + n\,\psi_{H,i}\big)\big)\right| \tag{106}$$

and

$$P_{V,i} \triangleq \left|\sum_{m=0}^{M-1}\sum_{n=0}^{N-1}\hat{H}_{m,n}^{(\mathrm{AE})}\exp\big(j2\pi\big(m\,\psi_{V,i} + n\,\psi_{H,2}\big)\big)\right| \tag{107}$$

are used in place of $P_{\rho,i}$ (103) and $P_{D,i}$ (102), respectively. A schematic description of Alg-P is provided in [30, Sec. 3, Tables 1 and 2].

D. MODIFIED FAN ALGORITHM

The fourth FFT-based method (namely, the MFA) results from: 1) adapting the estimation algorithm devised in [33] to the signal model expressed by (58); 2) including zero-padding in the initialization of the 2D periodogram method (see Section IV-A). The processing accomplished by the proposed algorithm evolves through the following two consecutive steps; note that, in this case, an estimate, denoted $\hat{K}$, of the overall number of targets is required.

1) 2D *periodogram maximization* - In this step the 2D periodogram is maximized (see our description of the 2D periodogram method in Section IV-A) in order to evaluate the *coarse estimates* $\hat{F}_{D_k,c}$ and $\hat{F}_{\rho_k,c}$ of the normalized Doppler frequency F_{D_k}, in (35), and the normalized range frequency F_{ρ_k}, in (36), respectively, with $k = 0, 1, \ldots, \hat{K}-1$.

2) *Frequency refinement* - First, the *fine estimates* of normalized Doppler frequency F_{D_k} and the normalized range frequency F_{ρ_k} are evaluated as

$$\hat{F}_{D_k} = \hat{F}_{D_k,c} - \hat{\Delta}_{D_k} \tag{108}$$

and

$$\hat{F}_{\rho_k} = \hat{F}_{\rho_k,c} + \hat{\Delta}_{\rho_k} \tag{109}$$

respectively, where

$$\big(\hat{\Delta}_{D_k}, \hat{\Delta}_{\rho_k}\big) \triangleq \underset{\left(\tilde{\Delta}_{D_k},\tilde{\Delta}_{\rho_k}\right)\in\mathcal{I}_D(M_0)\times\mathcal{I}_\rho(N_0)}{\arg\max} J_k\big(\tilde{\Delta}_{D_k}, \tilde{\Delta}_{\rho_k}\big), \tag{110}$$

with $k = 0, 1, \ldots, \hat{K}-1$, $\tilde{\Delta}_{D_k}$ ($\tilde{\Delta}_{\rho_k}$) represents the trial variable for the residual Δ_{D_k} (Δ_{ρ_k}), $\mathcal{I}_D(M_0)$ ($\mathcal{I}_\rho(N_0)$) is the *search domain* for Δ_{D_k} (Δ_{ρ_k}),

$$J_k\left(\tilde{\Delta}_{D_k}, \tilde{\Delta}_{\rho_k}\right) \triangleq \left\| \mathbf{f}_M^H\left(\hat{F}_{D_k,c}\right) \Phi_M\left(\tilde{\Delta}_{D_k}\right) \hat{\mathbf{H}}^{(\mathrm{RDE})} \Phi_N\left(\tilde{\Delta}_{\rho_k}\right) \mathbf{g}_N\left(\hat{F}_{\rho_k,c}\right) \right\|^2 \tag{111}$$

is the cost function selected for the considered estimation problem (see [33, Sec. III, eq. (31)]),

$$\mathbf{f}_M(F_D) \triangleq \frac{1}{M}\left[\exp(j2\pi(M/2)F_D), \ldots, 1, \exp(-j2\pi F_D), , \ldots, \exp(-j2\pi(M/2-1)F_D)\right]^T, \tag{112}$$

$$\mathbf{g}_N(F_\rho) \triangleq \frac{1}{N}\left[1, \exp\left(j2\pi F_\rho\right), \ldots, \exp\left(j2\pi(N-1)F_\rho\right)\right]^T \tag{113}$$

and

$$\Phi_X\left(\Delta_{Q_k}\right) \triangleq \mathrm{diag}\left\{\left[1, \exp\left(j2\pi\Delta_{Q_k}\right), \ldots, \exp\left(j2\pi\left(X-1\right)\Delta_{Q_k}\right)\right]\right\}, \tag{114}$$

with $Q = D$ ($Q = \rho$) if $X = M$ (if $X = N$). Then, the estimate

$$\hat{A}_k \triangleq \mathbf{f}_M^H\left(\hat{F}_{D_k}\right) \hat{\mathbf{H}}^{(\mathrm{RDE})} \mathbf{g}_N\left(\hat{F}_{\rho_k}\right) \tag{115}$$

of the complex amplitude characterizing the kth target is evaluated (with $k = 0, 1, \ldots, \hat{K}-1$). It is important to point out that the search domain $\mathcal{I}_D(M_0)$ ($\mathcal{I}_\rho(N_0)$) selected in our computer simulations consists of N_{F_D} (N_{F_ρ}) equally spaced numbers belonging to the interval $[-1/M_0,\ 1/M_0]$ ($[-1/N_0,\ 1/N_0]$); this interval covers two adjacent bins of the periodogram computed in the initialization of the algorithm.

The use of the MFA in the AE block requires the following changes:

1) The 2D periodogram method processes the spectral matrix $\mathbf{Y}^{(\mathrm{AE})}$, in (68), (in place of $\mathbf{Y}^{(\mathrm{RDE})}$, in (59)) to produce the *coarse estimates* $\hat{F}_{H_k,c}$ and $\hat{F}_{V_k,c}$ of the normalized frequencies F_{H_k} (33) and F_{V_k} (34), respectively (with $k = 0, 1, \ldots, \hat{K}-1$).

2) The *fine estimates* of F_{H_k} and F_{V_k} are evaluated as $\hat{F}_{H_k} = \hat{F}_{H_k,c} + \hat{\Delta}_{H_k}$ and $\hat{F}_{V_k} = \hat{F}_{V_k,c} + \hat{\Delta}_{V_k}$, respectively. The estimates of the residuals $\hat{\Delta}_{H_k}$ and $\hat{\Delta}_{V_k}$ represent the solution of an optimization problem formally identical to (110), where, however, $J_k(\tilde{\Delta}_{D_k}, \tilde{\Delta}_{\rho_k})$ is replaced by

$$J_k\left(\tilde{\Delta}_{V_k}, \tilde{\Delta}_{H_k}\right) \triangleq \left\| \mathbf{f}_M^H\left(\hat{F}_{V_k,c}\right) \Phi_M\left(\Delta_{V_k}\right) \hat{\mathbf{H}}^{(\mathrm{AE})} \Phi_N\left(\Delta_{H_k}\right) \mathbf{f}_N\left(\hat{F}_{H_k,c}\right) \right\|^2, \tag{116}$$

where

$$\mathbf{f}_X(F_Q) \triangleq \frac{1}{X}\left[\exp\left(-j2\pi(X/2)F_Q\right), \ldots, 1, \exp\left(j2\pi F_Q\right), \ldots, \exp\left(j2\pi(X/2-1)F_Q\right)\right]^T, \tag{117}$$

with $Q = V$ ($Q = H$) if $X = M$ (if $X = N$). Finally, the estimate

$$\hat{A}_k \triangleq \mathbf{f}_M^H\left(\hat{F}_{V_k}\right) \hat{\mathbf{H}}^{(\mathrm{AE})} \mathbf{f}_N\left(\hat{F}_{H_k}\right) \tag{118}$$

of the complex amplitude characterizing the kth target is evaluated (with $k = 0, 1, \ldots, \hat{K}-1$).

The MFA is summarized in Algorithm 3.

Algorithm 3: Modified Fan Algorithm (MFA)

Input: The matrix $\hat{\mathbf{H}}^{(\mathrm{RDE})}$ ($\hat{\mathbf{H}}^{(\mathrm{AE})}$) if the RDE (AE) is considered and an estimate of the overall number of targets ($\hat{K}$).

1 **Initialization:**

a-Compute the coarse estimates $\hat{F}_{D_k,c}$ and $\hat{F}_{\rho_k,c}$ ($\hat{F}_{V_k,c}$ and $\hat{F}_{H_k,c}$), if the RDE (AE) is considered, by resorting the 2D periodogram method.

2 **Refinement procedure:**

for $k = 0$ *to* $\hat{K}-1$ **do**

b-Compute the *fine estimates* $\hat{F}_{D_k} = \hat{F}_{D_k,c} - \hat{\Delta}_{D_k}$ and $\hat{F}_{\rho_k} = \hat{F}_{\rho_k,c} + \hat{\Delta}_{\rho_k}$ ($\hat{F}_{H_k} = \hat{F}_{H_k,c} + \hat{\Delta}_{H_k}$ and $\hat{F}_{V_k} = \hat{F}_{V_k,c} + \hat{\Delta}_{V_k}$) if the RDE (AE) is considered. The quantities $(\hat{\Delta}_{D_k}, \hat{\Delta}_{\rho_k})$ ($(\hat{\Delta}_{H_k}, \hat{\Delta}_{V_k})$) result from solving the optimization problem (110) with the cost function (111) (116) for the RDE (AE).

c-Compute the amplitude estimate $\hat{A}_k$ through (115) (118) for the RDE (AE).

end

Output: The set of estimates $\{(\hat{F}_{D_k}, \hat{F}_{\rho_k}, \hat{A}_k);\ k = 0, 1, ..., \hat{K}-1\}$ ($\{(\hat{F}_{H_k}, \hat{F}_{V_k}, \hat{A}_k);\ k = 0, 1, ..., \hat{K}-1\}$) for the RDE (AE).

E. Q-SHIFT ESTIMATOR

The fifth FFT-based algorithm (namely, the QSE) has been proposed by [31] to estimate the frequency of a 2D complex tone in the presence of AWGN. Similarly to the MFA, this estimator makes use of the 2D periodogram method for coarse frequency estimation and requires prior knowledge of the overall number of targets; however, it exploits a different method for frequency refinement. In fact, the last task is accomplished by a serial procedure that requires the evaluation of the DFT coefficients located at the relevant frequency bins shifted by a quantity $q \in [-0.5, 0.5]$. In practice, the final estimates of the normalized frequencies F_{D_k} (35) and F_{ρ_k} (36) are evaluated as

$$\hat{F}_{Q_k} = \hat{F}_{Q_k,c} + \hat{\delta}_{Q_k}/X, \tag{119}$$

with $Q = D$ ($Q = \rho$) if $X = M$ (if $X = N$); here, $\hat{F}_{Q_k,c}$ is a coarse estimate of F_{Q_k} and $\hat{\delta}_{Q_k}$ is an estimate of the associated residual. In the QSE, $\hat{F}_{D_k,c}$ ($\hat{F}_{\rho_k,c}$) is evaluated according to (64), (65) with $l = \hat{l}_k^{(\mathrm{RDE})}$ (with $p = \hat{p}_k^{(\mathrm{RDE})}$) and the couple $(\hat{l}_k^{(\mathrm{RDE})}, \hat{p}_k^{(\mathrm{RDE})})$ is provided by the 2D periodogram method for the RDE (see Section IV-A). The estimation of the residuals $(\hat{\delta}_{D_k}, \hat{\delta}_{\rho_k})$, instead, is accomplished by an iterative procedure; this is initialized by setting the initial estimates of the residuals (namely, $\hat{\delta}_{D_k}^{(0)}$ and $\hat{\delta}_{\rho_k}^{(0)}$) to zero and the iteration index i to 1. In the ith

iteration (with $i = 1, 2, \ldots, N_{\text{it}}$, where N_{it} is the overall number of iterations), the new estimate of the residual $\hat{\delta}_{X_k}^{(i)}$ is computed as

$$\hat{\delta}_{X_k}^{(i)} = \hat{\delta}_{X_k}^{(i-1)} + \frac{1}{c_X(q_X)} \Re\left\{ \frac{S_{+q_X}^{(i)} - S_{-q_X}^{(i)}}{S_{+q_X}^{(i)} + S_{-q_X}^{(i)}} \right\}, \tag{120}$$

with $X = D$ or ρ, and $k = 0, 1, \ldots, \hat{K} - 1$; here, $\hat{K}$ denotes our estimate of K,

$$S_{\pm q_D}^{(i)} \triangleq \sum_{m=0}^{M-1} \sum_{n=0}^{N-1} \hat{H}_{m,n}^{(\text{RDE})} \exp\left(-j2\pi \left(m\Upsilon_{\pm 1, q_D} - n\Upsilon_{0,q_\rho}\right)\right) \tag{121}$$

and

$$S_{\pm q_\rho}^{(i)} \triangleq \sum_{m=0}^{M-1} \sum_{n=0}^{N-1} \hat{H}_{m,n}^{(\text{RDE})} \exp\left(-j2\pi \left(m\Upsilon_{0, q_D} - n\Upsilon_{\pm 1,q_\rho}\right)\right) \tag{122}$$

are the DFT coefficients evaluated with small shifts (quantified by the real parameters q_D and q_ρ) with respect to the periodogram peak associated with the couple $(\hat{l}_k^{(\text{RDE})}, \hat{p}_k^{(\text{RDE})})$. Moreover,

$$\Upsilon_{z,q_D} \triangleq \left(\hat{l}_k^{(\text{RDE})} \bar{F}_D + \frac{\hat{\delta}_{D_k}^{(i-1)} + z q_D}{M} \right) \tag{123}$$

and

$$\Upsilon_{z,q_\rho} \triangleq \left(\hat{p}_k^{(\text{RDE})} \bar{F}_\rho + \frac{\hat{\delta}_{\rho_k}^{(i-1)} + z q_\rho}{N} \right) \tag{124}$$

are the normalized frequencies associated with the shifts q_D and q_ρ, respectively, z is an integer belonging to the set $\{0, \pm 1\}$, and

$$c_D(q_D) \triangleq \frac{1 - \pi q_D \cot(\pi q)}{q \cos^2(\pi q)} \tag{125}$$

and

$$c_\rho(q_\rho) \triangleq \frac{2\pi}{\sin(2\pi q_\rho)} \tag{126}$$

are correction factors. The final estimates of the residuals ($\hat{\delta}_{D_k}$ and $\hat{\delta}_{\rho_k}$) are evaluated as $\hat{\delta}_{D_k} = \hat{\delta}_{D_k}^{(N_{\text{it}})}$ and $\hat{\delta}_{\rho_k} = \hat{\delta}_{\rho_k}^{(N_{\text{it}})}$, respectively.

The use of the QSE in the AE requires the following modifications:

1) The final estimates of the normalized frequencies F_{H_k} and F_{Vk} are evaluated through (119), where $X = N$ ($X = M$) if $Q = H$ (if $Q = V$). Moreover, the coarse estimate $\hat{F}_{H_k,c}$ ($\hat{F}_{V_k,c}$) appearing in that formula is evaluated on the basis of (72), (73) with $p = \hat{p}_k^{(\text{AE})}$ (with $l = \hat{l}_k^{(\text{AE})}$); here, $(\hat{l}_k^{(\text{AE})}, \hat{p}_k^{(\text{AE})})$ denotes the couple of spectral indexes provided by the 2D periodogram method for the AE (see Section IV-A).

2) The computation of the residuals $\hat{\delta}_{H_k}$ and $\hat{\delta}_{V_k}$ is still based on (120) (with $X = H$ or V), but (122) and (121) are replaced by

$$S_{\pm q_H}^{(i)} \triangleq \sum_{m=0}^{M-1} \sum_{n=0}^{N-1} \hat{H}_{m,n}^{(\text{AE})} \exp\left(j2\pi \left(m\Psi_{0,q_V} + n\Psi_{\pm 1,q_H}\right)\right), \tag{127}$$

and

$$S_{\pm q_V}^{(i)} \triangleq \sum_{m=0}^{M-1} \sum_{n=0}^{N-1} \hat{H}_{m,n}^{(\text{AE})} \exp\left(j2\pi \left(m\Psi_{\pm 1,q_V} + n\Psi_{0,q_H}\right)\right) \tag{128}$$

respectively; here,

$$\Psi_{z,q_H} \triangleq \left(\hat{p}_k^{(\text{RDE})} \bar{F}_H + \frac{\hat{\delta}_{H_k}^{(i-1)} + z q_H}{N} \right) \tag{129}$$

and

$$\Psi_{z,q_V} \triangleq \left(\hat{l}_k^{(\text{RDE})} \bar{F}_V + \frac{\hat{\delta}_{V_k}^{(i-1)} + z q_V}{M} \right) \tag{130}$$

are the normalized frequencies associated with the shifts q_H and q_V, respectively, and z is an integer belonging to the set $\{0, \pm 1\}$. Moreover, the correction factors $c_X(q_X)$ (with $X = H$ or V) are both computed according to (126).

A schematic description of the QSE is provided in [31, Sec. IV, Algorithm 2].

F. EXTENDED LEE ALGORITHM

The last algorithm (namely, the ELA) has been originally proposed in [27, Sec. III] to perform azimuth estimation in a MIMO radar equipped with a *uniform linear array* (ULA) and is based on an ML approach. However, in our work, the following modifications have been made:

1) The original algorithm, being developed to estimate the frequencies of 1D tones, has been adapted to the 2D signal model expressed by (58), so making its use possible in both the RDE and the AE.

2) An iterative procedure for frequency refinement has been added. In each iteration of this procedure, the grid adopted in the search for the frequency estimate of a given target is adjusted to improve the achieved accuracy.

3) The 2D periodogram method has been employed for the initialization of the ELA; in the original algorithm, instead, the frequency estimates are initialized to zero for all the detected targets.

The ELA is fed by the 2D sequence $\{\hat{H}_{m,n}^{(\text{RDE})}\}$; in its initialization, this sequence is processed by the 2D periodogram method to evaluate the initial estimates $\hat{F}_{D_k}^{(0)}$, $\hat{F}_{\rho_k}^{(0)}$ and $\hat{A}_k^{(0)}$ of F_{D_k}, F_{ρ_k} and A_k, respectively, with $k = 0, 1, \ldots, \hat{K} - 1$ (being $\hat{K}$ a preliminary estimate of the overall number of targets K), and the iteration index i is set to one. Then, the refinement procedure is started. In its ith iteration (with

$i = 1, 2, \ldots, N_{\text{it}}$, where N_{it} is the overall number of iterations), the new estimates $\hat{F}_{D_k}^{(i)}$ and $\hat{F}_{\rho_k}^{(i)}$ of F_{D_k} and F_{ρ_k}, respectively, are evaluated as

$$\left(\hat{F}_{D_k}^{(i)}, \hat{F}_{\rho_k}^{(i)}\right) = \underset{\substack{\left(\tilde{F}_{D_k}, \tilde{F}_{\rho_k}\right) \\ \in \mathcal{I}_{F_D}^{(i)}(N_{F_D}) \times \mathcal{I}_{F_\rho}^{(i)}\left(N_{F_\rho}\right)}}{\arg\max} \left|J^{(i)}\left(\tilde{F}_{D_k}, \tilde{F}_{\rho_k}\right)\right|^2, \tag{131}$$

with $k = 0, 1, \ldots, \hat{K} - 1$; here,

$$J^{(i)}\left(\tilde{F}_{D_k}, \tilde{F}_{\rho_k}\right) \triangleq \frac{\mathbf{a}\left(\tilde{F}_{D_k}, \tilde{F}_{\rho_k}\right)^H \mathbf{R}^{-1} \bar{\mathbf{H}}}{\mathbf{a}\left(\tilde{F}_{D_k}, \tilde{F}_{\rho_k}\right)^H \mathbf{R}^{-1} \mathbf{a}\left(\tilde{F}_{D_k}, \tilde{F}_{\rho_k}\right)} \tag{132}$$

is the ML cost function evaluated for the trial couple $(\tilde{F}_{D_k}, \tilde{F}_{\rho_k})$, $\mathbf{a}(\tilde{F}_{D_k}, \tilde{F}_{\rho_k}) \triangleq \mathbf{a}(\tilde{F}_{D_k}) \otimes \mathbf{a}(-\tilde{F}_{\rho_k})$,

$$\mathbf{a}_Q(F_X) \triangleq \left[1, \exp(j2\pi F_X), \ldots, \exp(j2\pi(Q-1)F_X)\right]^T \tag{133}$$

is a *steering vector*, $\bar{\mathbf{H}} \triangleq [\mathbf{H}_0, \mathbf{H}_1, \ldots, \mathbf{H}_{M-1}]$ is a (MN)-dimensional row vector, $\mathbf{H}_m \triangleq [\hat{H}_{m,0}^{(\text{RDE})}, \hat{H}_{m,1}^{(\text{RDE})}, \ldots, \hat{H}_{m,N-1}^{(\text{RDE})}]$ (with $m = 0, 1, \ldots, M-1$) and $\mathbf{R} = \sigma_H^2 \mathbf{I}_{MN}$ represents the covariance matrix of the Gaussian measurement noise, whose samples have variance σ_H^2 ($\sigma_H^2 = MN$ can be selected as the first attempt guess of the noise variance of $\bar{\mathbf{H}}$; see [27, Sec. (III), eq. (21)]). Moreover, the search grid in (131) results from the Cartesian product of the sets[18] $\mathcal{I}_{F_D}^{(i)}(N_{F_D}) \triangleq \{\tilde{F}_D^{(i)}[z_D];\ z_D = 0, 1, \ldots, N_{F_D} - 1\}$ and $\mathcal{I}_{F_\rho}^{(i)}(N_{F_\rho}) \triangleq \{\tilde{F}_\rho^{(i)}[z_\rho];\ z_\rho = 0, 1, \ldots, N_{F_\rho} - 1\}$. This grid has the following relevant properties: 1) its center depends on both $\hat{F}_{D_k}^{(i-1)}$ and $\hat{F}_{\rho_k}^{(i-1)}$; 2) its step sizes get smaller as i increases. More precisely, its node (z_D, z_ρ) (with $z_D = 0, 1, \ldots, N_{F_D} - 1$ and $z_\rho = 0, 1, \ldots, N_{F_\rho} - 1$) is associated with the frequencies $(\tilde{F}_D^{(i)}[z_D], \tilde{F}_\rho^{(i)}[z_\rho])$, where

$$\tilde{F}_X^{(i)}[z_X] = F_{X,\min} + \left(z_X / \left(N_{F_X} - 1\right)\right)(\delta_X / i), \tag{134}$$

if $F_{X,\min} \le \hat{F}_{X_k}^{(i-1)} < F_{X,\min} + \delta_X$,

$$\tilde{F}_X^{(i)}[z_X] = \hat{F}_{X_k}^{(i-1)} + \left(\left(z_X / \left(N_{F_X} - 1\right)\right) - 1/2\right)(\delta_X / i), \tag{135}$$

if $F_{X,\min} + \delta_X \le \hat{F}_{X_k}^{(i-1)} \le F_{X,\max} - \delta_X$ and

$$\tilde{F}_X^{(i)}[z_X] = F_{X,\max} + \left(\left(z_X / \left(N_{F_X} - 1\right)\right) - 1\right)(\delta_X / i), \tag{136}$$

if $F_{X,\max} - \delta_X < \hat{F}_{X_k}^{(i-1)} \le F_{X,\max}$, with $X = D$ or ρ. Moreover, $\delta_X = 1/M_0$ ($\delta_X = 1/N_0$) is selected if $X = D$ (if $X = \rho$), so that, when $i = 1$, two adjacent bins of the spectrum considered in coarse frequency estimation are covered.

18. The dependence of $\mathcal{I}_{F_D}^{(i)}$, $\mathcal{I}_{F_\rho}^{(i)}$ and $\tilde{F}_X^{(i)}[z]$ on the target index k is not shown in the following three equations to ease notation.

Algorithm 4: Extended Lee Algorithm (ELA)

Input: The matrix $\hat{\mathbf{H}}^{(\text{RDE})}$ ($\hat{\mathbf{H}}^{(\text{AE})}$) for the RDE (AE), the overall number of iterations in frequency refinement (N_{it}) and an estimate of the overall number of targets ($\hat{K}$).

Initialization: Evaluate the estimates $(\hat{F}_{D_k}^{(0)}, \hat{F}_{\rho_k}^{(0)}, \hat{A}_k^{(0)})$ $(\hat{F}_{H_k}^{(0)}, \hat{F}_{V_k}^{(0)}, \hat{A}_k^{(0)})$ by finding $\hat{K}$ peaks in the spectrum (61) (69) for the RDE (AE).

Refinement: for $k = 0$ *to* $\hat{K} - 1$ **do**

  for $i = 1$ *to* N_{it} **do**

    a-Compute the estimates $(\hat{F}_{D_k}^{(i)}, \hat{F}_{\rho_k}^{(i)})$ $(\hat{F}_{V_k}^{(i)}, \hat{F}_{H_k}^{(i)})$ by means of (131).

  end

  b-Evaluate the kth target amplitude as $\hat{A}_k = J^{(N_{\text{it}})}(\hat{F}_{D_k}^{(N_{\text{it}})}, \hat{F}_{\rho_k}^{(N_{\text{it}})})$ for the RDE or $\hat{A}_k = J^{(N_{\text{it}})}(\hat{F}_{V_k}^{(N_{\text{it}})}, \hat{F}_{H_k}^{(N_{\text{it}})})$ for the AE (see (132)).

end

Output: The estimates $(\hat{F}_{D_k}^{(N_{\text{it}})}, \hat{F}_{\rho_k}^{(N_{\text{it}})}, \hat{A}_k^{(i)})$ $((\hat{F}_{H_k}^{(N_{\text{it}})}, \hat{F}_{V_k}^{(N_{\text{it}})}, \hat{A}_k^{(N_{\text{it}})}))$ for the kth target (with $k = 0, 1, ..., \hat{K} - 1$) if the RDE (AE) is considered.

At the end of the last (namely, the N_{it}th) iteration, an estimate of the complex amplitude of the kth target is evaluated as $\hat{A}_k = J^{(N_{\text{it}})}(\hat{F}_{D_k}^{(N_{\text{it}})}, \hat{F}_{\rho_k}^{(N_{\text{it}})})$ (see (132)).

The ELA can also be employed in the AE; its formulation for the last block can be easily derived from that illustrated above for the RDE by simply replacing $\hat{H}_{m,n}^{(\text{RDE})}$, F_D and F_ρ with $\hat{H}_{m,n}^{(\text{AE})}$, $-F_V$ and F_H, respectively.

The ELA is summarized in Algorithm 4.

V. COMPUTATIONAL COMPLEXITY

In this section, the computational cost of the DRAEC strategy and of the estimation algorithms exploited by it is analyzed in terms of the *floating point operations* (FLOPs) to be executed when K targets are detected and estimated. In general, the complexity of the DRAEC technique is approximately of order $\mathcal{O}(N_{\text{DRAEC}})$, where

$$N_{\text{DRAEC}} = N_{\text{RDE}} + N_{\text{CAE}} + N_{\text{AE}} + N_{\text{CRDE}} + \bar{N}_{\text{RDE}}. \tag{137}$$

In the last formula, the terms N_{RDE} and N_{AE} represent the number of FLOPs required by the RDE and the AE, respectively, whereas $\bar{N}_{\text{RDE}}$ refers to the number of FLOPs required by the second instance of the RDE for the refinement of the range-Doppler estimates. Moreover, $N_{\text{CAE}} = 4KMNN_TN_R$ and $N_{\text{CRDE}} = 4KMNN_TN_R$ represent the costs due to range-Doppler and angular compensation through (49) and (53), respectively. The expressions of the terms N_{RDE}, N_{AE} and $\bar{N}_{\text{RDE}}$ depend on the choice of the detection & estimation algorithm employed by the RDE and AE; our main results about the computational complexity of the algorithms described in the previous section are summarized below.

2D *periodogram method* - The computational complexity of this method is $\mathcal{O}(\mathcal{C}_{2D-FFT})$, where

$$\mathcal{C}_{2D-FFT} = M_0 N_0 \log_2(M_0 N_0) + K M_0 N_0. \tag{138}$$

If spectral interpolation is used, the term

$$\mathcal{C}_{int} = K\left(I_l I_p + N_l N_p\right) \tag{139}$$

has to be added to $\mathcal{C}_{2D-FFT}$, in (138); here, I_l (I_p) is the number of nodes employed along the first (second) dimension, whereas N_l (N_p) is the resulting number of points evaluated by means of interpolation for the first (second) dimension.

CSFDEC *algorithm* - The computational complexity of this method is $\mathcal{O}(C_{\text{CSFDEC}})$, where (see [32, Sec. III-C])

$$C_{\text{CSFDEC}} = 13 M_0 N_0 \log_2(M_0 N_0) + 13 K^2 N_{\text{REF}} N_{\text{it}} I_M I_N. \tag{140}$$

In the last formula, N_{REF}, N_{it}, I_M (I_N) are the overall number of re-estimations, the overall number of iterations accomplished in the evaluation of the residuals appearing in (86) and the interpolation order adopted for the first (second) dimension of the considered spectrum in (77), respectively.

Alg-P - Unlike the CSFDEC algorithm, this algorithm does not operate in an iterative fashion, performs *time domain* cancellation and re-computes the spectral residual after each cancellation step in order to get ready for the detection of a new target (if any). For these reasons, its computational complexity is $\mathcal{O}(C_{\text{ALG-P}})$, where

$$C_{\text{ALG-P}} = K(C_{\text{init}} + C_P + C_{\text{canc}}). \tag{141}$$

In the last formula, $C_{\text{init}} = M_0 N_0 \log_2(M_0 N_0) + M_0 N_0$ is the contribution due to step 1) of Alg-P (i.e., to the 2D *periodogram maximization*), $C_P = C_{P_M} + C_{P_N}$ (with $C_{P_M} = C_{P_N} = 12MN$) is the cost originating from the computation of the spectral samples for the first and second frequency of the kth target (see (102) and (103), respectively) and $C_{\text{canc}} = KMN$ is the contribution due to cancellation in the time domain. Note that the initialization cost depends on the number of targets K; this is due to the fact that the residual spectrum for the coarse estimation of a new target is evaluated after each time domain cancellation (see (94)).

MFA - The initialization phase of this algorithm relies, similarly as both the CSFDEC algorithm and the Alg-P, on the 2D periodogram method; however, since the MFA does not include a cancellation procedure, the search for K local maxima in the periodogram is required in order to acquire K coarse frequency estimates. Moreover, the initialization is followed by a frequency refinement process, which is sequentially repeated for each target. Therefore, the computational complexity of the MFA is $\mathcal{O}(C_{\text{MFA}})$, where

$$C_{\text{MFA}} = C_{\text{init}} + K C_{\text{ref}}. \tag{142}$$

In the last formula, C_{init} is equal to $\mathcal{C}_{2D-FFT}$, in (138), (initialization cost) and $C_{\text{ref}} = 16MNN_{F_D}N_{F_\rho}$ ($C_{\text{ref}} = 16MNN_{F_V}N_{F_H}$) is the cost of the refinement step, being N_{F_D} and N_{F_ρ} (N_{F_V} and N_{F_H}) the number of trial values characterizing the grid selected for F_D and F_ρ (F_V and F_H) if the RDE (AE) is considered.

QSE - Similarly to the MFA and the ELA, this algorithm evaluates first the coarse estimates of K targets through the 2D periodogram method. The frequency refinement step requires evaluating (120) N_{it} times for each target. Therefore, the computational complexity of the QSE is $\mathcal{O}(C_{\text{QSE}})$, where

$$C_{\text{QSE}} = C_{\text{init}} + K N_{\text{it}} C_{\text{ref}}. \tag{143}$$

In the last formula, C_{init} is the initialization cost (which is equal to that of the same step of the MFA and the ELA), N_{it} represents the overall number of iterations carried out to evaluate (120) and $C_{\text{ref}} = 8MN$ is the complexity due to the computation of the DFT coefficients required to solve the last referred equation.

ELA - The initialization of this algorithm is based on the 2D periodogram method and is followed by the frequency refinement step, which requires solving (131) N_{it} times for each target. Therefore, the computational complexity of the ELA is $\mathcal{O}(C_{\text{ELA}})$, where

$$C_{\text{ELA}} = C_{\text{init}} + K N_{\text{it}} C_{\text{ref}}. \tag{144}$$

In the last formula, C_{init} is equal to $\mathcal{C}_{2D-FFT}$, in (138), (being the cost of 2D periodogram method), N_{it} is the number of iterations carried out to refine the estimates of each target and $C_{\text{ref}} = 16(M^2 + N^2 + MN)N_{F_D}N_{F_\rho}$ ($C_{\text{ref}} = 16(M^2 + N^2 + MN)N_{F_V}N_{F_H}$) represents the cost of each iteration of the refinement step, being N_{F_D} and N_{F_ρ} (N_{F_V} and N_{F_H}) the sizes of the grid for the refinement of F_D and F_ρ (F_V and F_H), respectively, if the RDE (AE) is considered.

VI. NUMERICAL RESULTS

In our work, seven different embodiments of the DRAEC strategy are compared in terms of computational effort and estimation accuracy achieved in various scenarios. In each embodiment, the same algorithm for the detection and estimation of 2D complex tones is employed in both the RDE and the AE, and the RDE is executed for the second time after that the AE has estimated the DoA (i.e., both the azimuth and the elevation) of all the detected targets in order to generate a finer estimate[19] of their range and velocity. For this reason, in the following, the acronyms FFT0 (FFTi), CSFDEC, Alg-P, MFA, QSE and ELA are adopted to identify the embodiments employing the 2D periodogram method *without spectral interpolation* (*with spectral interpolation*), the CSFDEC algorithm, the Alg-P, the MFA, the QSE and the ELA, respectively. It is important to point out that embedding these algorithms in the DRAEC allows us to compare state-of-the-art estimators, in terms of accuracy and complexity, in a 4D radar imaging problem and, in particular, to assess their performance in the estimation of specific parameters of multiple targets.

19. Note that the performance of the second instance of the RDE is affected by the estimation errors introduced by the AE.

In the following, we also assume that:

1) The considered radar system is equipped with a TX HULA (RX VULA) consisting of $N_T = 8$ ($N_R = 8$) elements, whose spacing, as already mentioned in Section II, is $d_t = \lambda/2$ ($d_r = \lambda/2$); consequently, the structure of its virtual array is described by Fig. 2.

2) The OFDM modulation employed by the radar system is characterized by the following parameters: a) overall number of subcarriers $N = 512$; b) overall number of OFDM symbols/frame $M = 64$; c) subcarrier spacing $\Delta_f = 250$ kHz; d) cyclic prefix duration $T_G = 12.5$ μs (consequently, the OFDM symbol duration is $T_s = 1/\Delta_f + T_G = 16.5$ μs); e) carrier frequency $f_c = 79$ GHz (consequently, the carrier wavelength is $\lambda = c/f_c = 3.8$ mm); f) cardinality of the PSK constellation $N_s = 4$.

In our simulations, four different scenarios have been considered. The first three scenarios share the following features:

1) They are characterized by a couple of targets (i.e., by $K = 2$), whose echoes have a unitary amplitude (so that $|A_0| = |A_1| = 1$). The range R_0, the velocity v_0, the normalized vertical frequency[20] F_{V_0} and the normalized horizontal frequency F_{H_0} of the first target are mutually independent and uniformly distributed random variables (the interval characterizing the uniform distribution of these variables is denoted $(X_{\min}, X_{\max})$ in the following, with $X = R$, v, F_V or F_H).[21] The same parameters for the second target (namely, R_1,v_1, F_{V_1} and F_{H_1}), instead, depend on those of the first one, since they are evaluated as

$$X_1 = X_0 + X_{\text{bin}}\, X_{\text{res}}, \tag{145}$$

where $X = R$, v, F_V or F_H, and X_{bin} and X_{res} represent the normalized target spacing and the resolution, respectively, of the radar system along the X dimension; moreover, $R_{\text{res}} = c/(2N\Delta_f) = 1.1719$ m, $v_{\text{res}} = \lambda/(2MT_s) = 1.798$ m/s, $F_{V_{\text{res}}} = 1/N_R = 0.125$ and $F_{H_{\text{res}}} = 1/N_T = 0.125$ denote the resolutions in the range, velocity, normalized vertical frequency and normalized horizontal frequency domains, respectively.

2) The *signal-to-noise ratio*[22]

$$\text{SNR} \triangleq \sum_{k=0}^{K-1} |A_k|^2/\sigma_W^2, \tag{146}$$

at the RX side varies from -20 to 20 dB.

However, the first three scenarios differ for the values selected for the parameters $X_{\min}$, $X_{\max}$ and X_{bin}, with $X = R$, v, F_V and F_H. In fact, we have that:

1) In the first scenario (denoted **S1**), $(R_{\min}, R_{\max}) = (0,\ 10)$ m, $(v_{\min}, v_{\max}) = (0,\ 2.78)$ m/s, $(F_{V_{\min}}, F_{V_{\max}}) = (0,\ 0.1754)$, $(F_{H_{\min}}, F_{H_{\max}}) = (-0.1761,\ 0.1761)$, $R_{\text{bin}} = v_{\text{bin}} = 3$ and $F_{V_{\text{bin}}} = F_{H_{\text{bin}}} = 2$.

2) In the second scenario (denoted **S2**), the intervals $(F_{V_{\min}}, F_{V_{\max}})$ and $(F_{H_{\min}}, F_{H_{\max}})$ are the same as **S1**, but $(R_{\min}, R_{\max}) = (10,\ 20)$ m, $(v_{\min}, v_{\max}) = (2.78,\ 5.56)$ m/s, $R_{\text{bin}} = v_{\text{bin}} = 0$ and $F_{V_{\text{bin}}} = F_{H_{\text{bin}}} = 2.2$.

3) In the third scenario (denoted **S3**), the intervals $(R_{\min}, R_{\max})$ and $(v_{\min}, v_{\max})$ are the same as **S2**, but $(F_{V_{\min}}, F_{V_{\max}}) = (0,\ 0.3566)$, $(F_{H_{\min}}, F_{H_{\max}}) = (-0.3623,\ 0.3623)$, $R_{\text{bin}} = v_{\text{bin}} = 3$ and $F_{V_{\text{bin}}} = F_{H_{\text{bin}}} = 0$.

The fourth scenario (denoted **S4**), instead, has the following characteristics:

1) Its overall number of targets is varying (in particular, $K \in \{1, 2, \ldots, 5\}$).

2) The range R_0, the velocity v_0, the normalized vertical frequency F_{V_0} and the normalized horizontal frequency F_{H_0} of the first target are mutually independent and uniformly distributed random variables; the intervals $(R_{\min}, R_{\max})$, $(v_{\min}, v_{\max})$ and $(F_{V_{\min}}, F_{V_{\max}})$ selected for R_0, v_0 and F_{V_0}, respectively, are the same as **S2**, whereas the interval $(F_{H_{\min}}, F_{H_{\max}}) = (-0.7765,\ -0.5534)$ is chosen for F_{H_0}.

3) The amplitude of the kth target (with $k = 0, 1, \ldots, K-1$) is unitary.

4) The range R_k, velocity v_k, normalized vertical frequency F_{V_k} and normalized horizontal frequency F_{H_k} of the kth target (with $k = 1, 2, \ldots, K-1$) are evaluated as $X_k = X_0 + k\, X_{\text{bin}}\, X_{\text{res}}$, with $X = R$, v, F_V or F_H (the parameters X_{bin} and X_{res} have been already defined; see (145)); here, $R_{\text{bin}} = v_{\text{bin}} = 1.8$ and $F_{V_{\text{bin}}} = F_{H_{\text{bin}}} = 0.7$.

5) The SNR is fixed and set to 10 dB. The selection of the four scenarios defined above can be motivated as follows. On the one hand, the first scenario allows us to compare the considered embodiments of the DRAEC strategy in the presence of two targets whose spacing in the range, velocity and angular domains is *fixed*, *but not small*. On the other hand, in the second (third) scenario, we still focus on the case of two targets, but assume that they are overlapped in range and velocity (azimuth and elevation) domains, whereas they are well spaced in the azimuth and elevation (range and velocity) domains. The fourth scenario, instead, allows us to assess the impact of a variable number of targets on the estimation accuracy; note that such targets are quite close in the azimuth and elevation domains, but are fairly spaced in the range and velocity domains.

In our simulations,[23] the following choices have been also made:

1) The overall number of targets (i.e., K) has been always assumed to be known. This entails that, none of the 2D estimators employed in the DRAEC strategy requires setting a specific threshold. Note, however, that the target configuration is unknown at the RX side; for instance, the radar receiver is unaware of the existence of targets characterized

20. Note that, given the normalized spatial frequencies F_V and F_H characterizing a given target, target elevation θ and azimuth ϕ can be easily computed on the basis of (33) and (34), respectively.

21. In all the scenarios, target parameters have been generated by means of the function *rand* available in MATLABR2022b.

22. Note that σ_W^2 represents the variance of the noise sample $\bar{W}_{m,n}^{(p_a,q)}$ appearing in the RHS of (40).

23. All the simulations have been performed on MATLAB R2022b, running on a personal computer equipped with an i7 processor.

by the same parameters in some domain (e.g., by the same DoA).

2) In the first three scenarios, the estimation accuracy achieved by each embodiment of the DRAEC strategy has been assessed by evaluating the *root mean square error* (RMSE)

$$\mathrm{RMSE}_X \triangleq \frac{1}{N_\mathrm{r}} \sum_{t=0}^{N_\mathrm{r}-1} \sqrt{\frac{1}{K} \sum_{k=0}^{K-1} \left(\hat{X}_k[t] - X_k \right)^2} \qquad (147)$$

for the range ($X = R$), velocity ($X = v$), azimuth ($X = \theta$) and elevation angle ($X = \phi$) of the considered targets; here, $\hat{X}_k[t]$ denotes the estimate of the parameter X_k evaluated for the kth target in the tth Monte Carlo run and N_r is the overall number of Monte Carlo runs. Moreover, in applying the last formula, the parameters of the K targets and the estimates generated for them have been ordered on the basis of their range (in particular, according to an ascending order, i.e., from minimum to maximum range).

3) In the fourth scenario, instead, the estimation accuracy achieved by each embodiment of the DRAEC strategy has been assessed by evaluating the *normalized* RMSE

$$\mathrm{NRMSE}_X \triangleq \frac{\mathrm{RMSE}_X}{\mathrm{CRLB}_X}, \qquad (148)$$

with $X = R$, v, F_V and F_H; here, CRLB_X denotes the *Cramer-Rao Lower Bound* (CRLB) for the estimation of X (the evaluation of the CRLB for the considered scenarios is illustrated in the Appendix-A). Note that the adoption of NRMSE_X, in (148), as a performance index allows us to fairly compare the estimation accuracy of each algorithm achieved in the presence of a variable number of targets and its computation is done for each SNR value.

4) The detection thresholds adopted in the inequalities (47) and (52) have not been selected, being K known. In practice, the RDE, in its first instance, searches for $K^{(\mathrm{RDE})} = K$ targets (i.e., K range-Doppler bins). Then, the AE identifies $K^{(\mathrm{AE})} \geq K$ targets, orders them according to a decreasing perceptual importance and discards the last $(K^{(\mathrm{AE})} - K)$ of them.

5) In all the considered scenarios, the oversampling factors $L_1^{(\mathrm{RDE})} = L_2^{(\mathrm{RDE})} = 4$ ($L_1^{(\mathrm{AE})} = L_2^{(\mathrm{AE})} = 8$) have been adopted for the RDE (for the AE), independently of the employed frequency estimation algorithm; consequently, according to (62), (63), (70), (71), we have that $M_0 = 512$ ($\bar{M}_0 = 64$) and $N_0 = 2048$ ($\bar{N}_0 = 64$).

In addition, in all the considered scenarios, the following choices have been made for the parameters of the 2D complex tone estimators.

2D *periodogram method with interpolation* - Orders $I_l = I_p = 7$ have been adopted for the spectral interpolation accomplished in both the RDE and the AE, and a grid of size $N_l \times N_p = 251 \times 251$ is selected in the serial refinement of the target estimates.

CSFDEC *algorithm* - Number of iterations carried out in the evaluation of the residuals $N_\mathrm{it}^{(\mathrm{RDE})} = 30$ ($N_\mathrm{it}^{(\mathrm{AE})} = 35$), number of re-estimations $N_\mathrm{REF}^{(\mathrm{RDE})} = 3$ ($N_\mathrm{REF}^{(\mathrm{AE})} = 3$) and interpolation orders along the two dimensions of the spectral components $I_M^{(\mathrm{RDE})} = I_N^{(\mathrm{RDE})} = 7$ ($I_M^{(\mathrm{AE})} = I_N^{(\mathrm{AE})} = 7$) for the RDE (for the AE).

MFA - Number of trial values employed in (111) (in (116)) $N_{F_D} = N_{F_\rho} = 51$ ($N_{F_V} = N_{F_H} = 51$) for the RDE (for the AE).

QSE - Number of iterations for frequency refinement $N_\mathrm{it}^{(\mathrm{RDE})} = 20$ ($N_\mathrm{it}^{(\mathrm{AE})} = 20$) and q-shifts $q_D = q_\rho = 0.031$ ($q_V = q_H = 0.25$) for the RDE (for the AE).

ELA - Number of iterations accomplished to refine target estimates $N_\mathrm{it}^{(\mathrm{RDE})} = 7$ ($N_\mathrm{it}^{(\mathrm{AE})} = 7$) and number of trial values employed in (132) $N_{F_D} = N_{F_\rho} = 15$ ($N_{F_V} = N_{F_H} = 15$) for the RDE (for the AE).

Some numerical results referring to **S1** are shown in Fig. 4, where the performance index RMSE_X (with $X = R$, v, θ or ϕ) characterizing all the considered algorithms is shown for SNR $\in [-20, 20]$ dB (in these figures and in all the following ones, simulation results are represented by labels, whereas continuous and dotted lines are drawn to ease reading). From these results, it is easily inferred that:

1) The FFT0 is outperformed by all the other methods; note also that the floor observed in the RMSE performance of this embodiment is due to the discretization of the grid (see (76)) employed in the RDE and in the AE (see (61) and (69), respectively).

2) The CSFDEC and the Alg-P achieve very good accuracy (close to the CRLB) thanks to their use of cancellation and refinement procedures.

3) The QSE performs similarly to the Alg-P (FFTi) in range (angle) estimation and similarly to the CSFDEC in velocity estimation.

4) The FFTi takes advantage of peak interpolation, so achieving an estimation accuracy similar to that of the MFA and of the ELA in angular estimation. These considerations, together with those illustrated at point 3), also apply to **S2** and **S3**.

5) The RMSE curves for the FFTi, the MFA and the ELA exhibit a floor at high SNRs. This is due to the fact that the accuracy of the FFTi estimator and the MFA is intrinsically limited by the discretization of their search grid. Further simulation results have evidenced that enlarging the set of trial values improves estimation accuracy; however, this result is achieved at the price of higher computational complexity. As far as the ELA is concerned, its accuracy can also be improved by increasing its number of iterations, but this results in a significant increase in the required computational effort. These considerations apply to all the results shown below for the three algorithms that have been just mentioned.

6) The RMSE_R and RMSE_v curves of the Alg-P exhibit a floor at high SNRs. This phenomenon can be related to the fact the employed estimation algorithm is biased, since it does not include neither an iterative refinement process nor a leakage compensation procedure for each detected target.

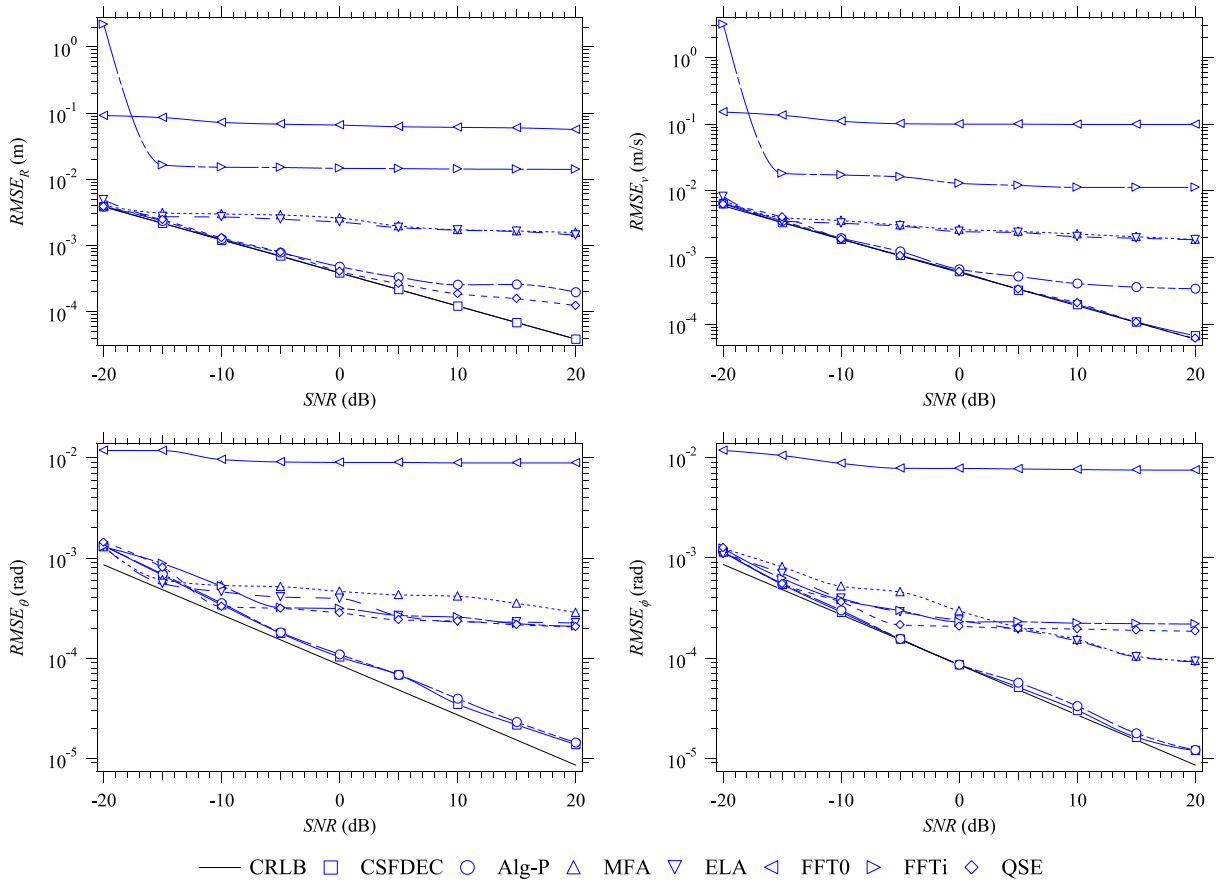

FIGURE 4. Root mean square error performance achieved by the considered embodiments of the DRAEC strategy. The first scenario is considered.

7) The computational efforts required by the FFTi, the CSFDEC, the Alg-P, the MFA, the QSE and the ELA are 1.01, 6.6, 1.1, 10, 1.2 and 49 times higher than that required by the FFT0; these results also hold for **S2** and **S3**.

Further results for **S1** are shown in Fig. 5, in which the RMSE_R curves of the CSFDEC, the Alg-P and the QSE are shown for the cases in which the RDE is executed only once (dashed lines) and twice (solid lines). From this figure, it is easily inferred that:

1) The improvement in range estimation provided by the second instance of the RDE in order is significant for all the proposed techniques; similar results, not shown here, have been found for velocity estimation.

2) The price to be paid for this improvement is an increase in the overall computational effort (this is quantified by the term $\bar{N}_{\mathrm{RDE}}$ appearing in (137)).

Note also that running a single instance of the RDE corresponds to what is done in all the related technical manuscripts in which only a subset of the target parameters (range and Doppler, in this case) is estimated, whereas the other parameters are kept fixed and/or are not successively compensated for (e.g., see [4] where the angular parameters are not estimated). For this reason, these results evidence the importance of estimating all the target parameters jointly.

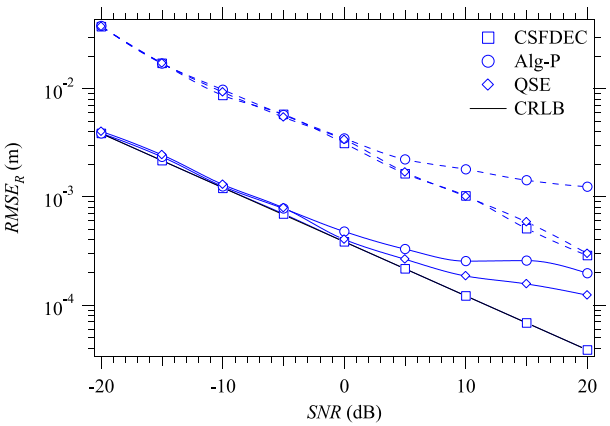

FIGURE 5. Root mean square error performance achieved in range estimation by the first and the second instance of the RDE. The first scenario and three different embodiments of the DRAEC strategy are considered.

Some numerical results referring to **S2** are shown Fig. 6, where the performance index RMSE_X (with $X = R$, v, θ or ϕ), characterizing all the considered algorithms, is shown for $\mathrm{SNR} \in [-20,\ 20]$ dB. These results lead to the following conclusions:

1) The FFTi, the MFA and the ELA achieve similar accuracy in the estimation of angular parameters and exhibits

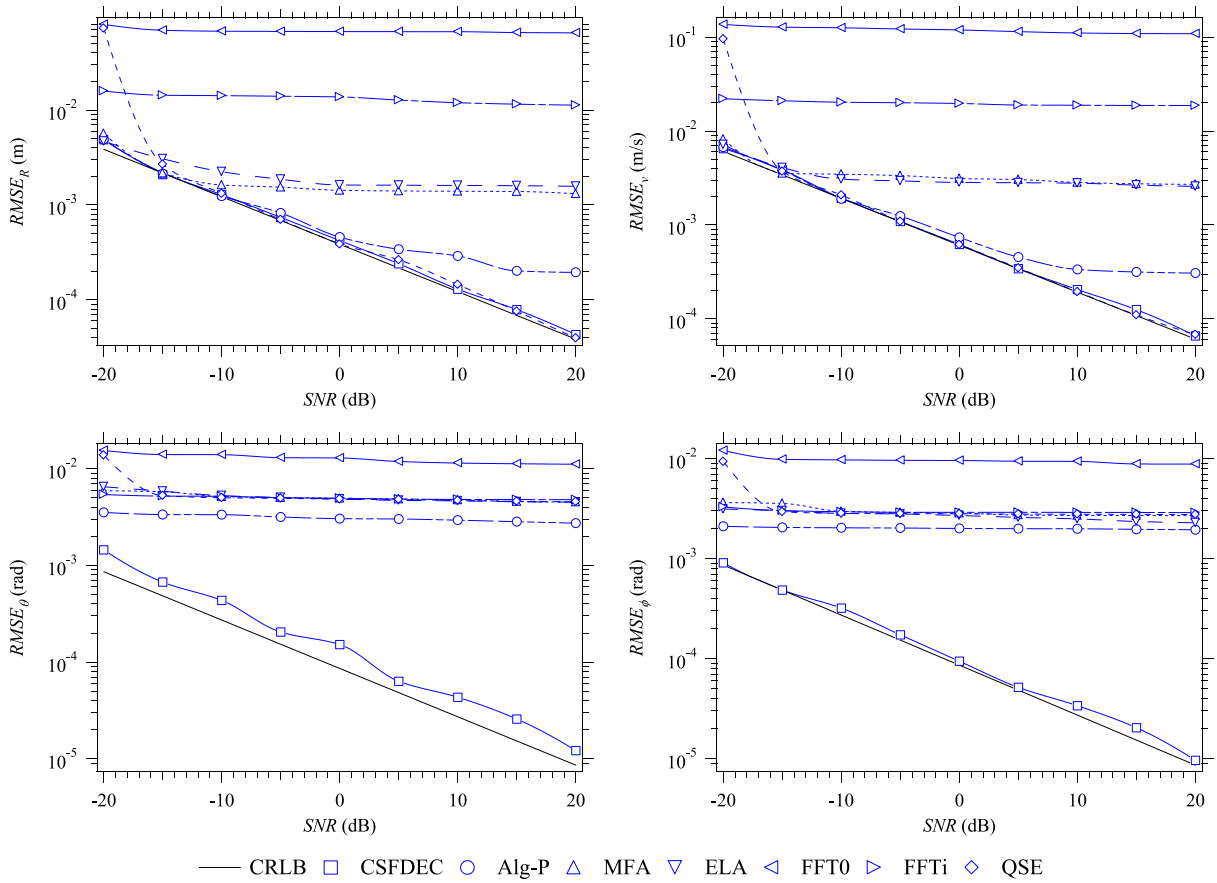

FIGURE 6. Root mean square error performance achieved by the considered embodiments of the DRAEC strategy. The second scenario is considered.

similar trends (and, in particular, a floor); however, the FFTi is outperformed by the MFA and the ELA in range and Doppler estimation.

2) The RMSE_θ and RMSE_ϕ referring to the Alg-P and the QSE are quite flat. This is due to the fact the two targets are located in the same range-Doppler bin. This affects the quality of the signal generated by the AE in compensating for the range and Doppler of each target (see (49)) and passed to the RDE. Moreover, the performance of the QSE is appreciably influenced by the selection of the shifting parameters (i.e., q_V and q_H for the AE). The values of these parameters have been optimized according to [31, Sec. III, eqs. (40) and (45)].

3) The CSFDEC performs substantially better than all the other embodiments in the estimation of azimuth and elevation, and similarly as the QSE in range and velocity estimation (the accuracy of both embodiments is very close to the CRLB).

Some numerical results obtained for **S3** are illustrated in Fig. 7, showing again the dependence of the RMSEs on the SNR, with $\text{SNR} \in [-20, 20]$ dB. These results lead to the following conclusions:

1) The CSFDEC and the QSE achieve the best estimation accuracy (very close to the CRLB) for all the considered parameters, whereas the Alg-P performs similarly in angle estimation only.

2) The accuracy provided by the MFA in azimuth and elevation estimation is slightly better than that characterizing the ELA and the FFTi.

3) The accuracy achieved by the MFA in range and velocity estimation is similar to that provided by the Alg-P and the ELA; moreover, the trend of their RMSE_R and RMSE_v curves remains flat even at high SNR values.

Our last results refer to **S4** and are shown in Figs. 8 and 9. In particular, in Fig. 8 the NRMSE characterizing all the considered embodiments at a given SNR and in the presence of a variable number of targets is shown. These results lead to the following conclusions:

1) The NRMSE_X increases with the overall number of targets (i.e., the RMSE_X departs from the associated CRLB), with $X = R$, v, F_V or F_H. This is due to the fact that increasing K results in a stronger spectral *leakage* and, consequently, in poorer estimation accuracy of each algorithm.

2) The CSFDEC, the Alg-P and the QSE perform similarly in range and velocity estimation, whereas the CSFDEC performs better in the estimation of azimuth and elevation. This confirms once again that the CSFDEC algorithm better exploits the limited information available in the angular domain[24] and takes advantage of its *leakage compensation* mechanism.

24. The estimation of angular parameters is based on the $N_T \times N_R$ matrix $\check{\mathbf{H}}_k$; see Section III-B.

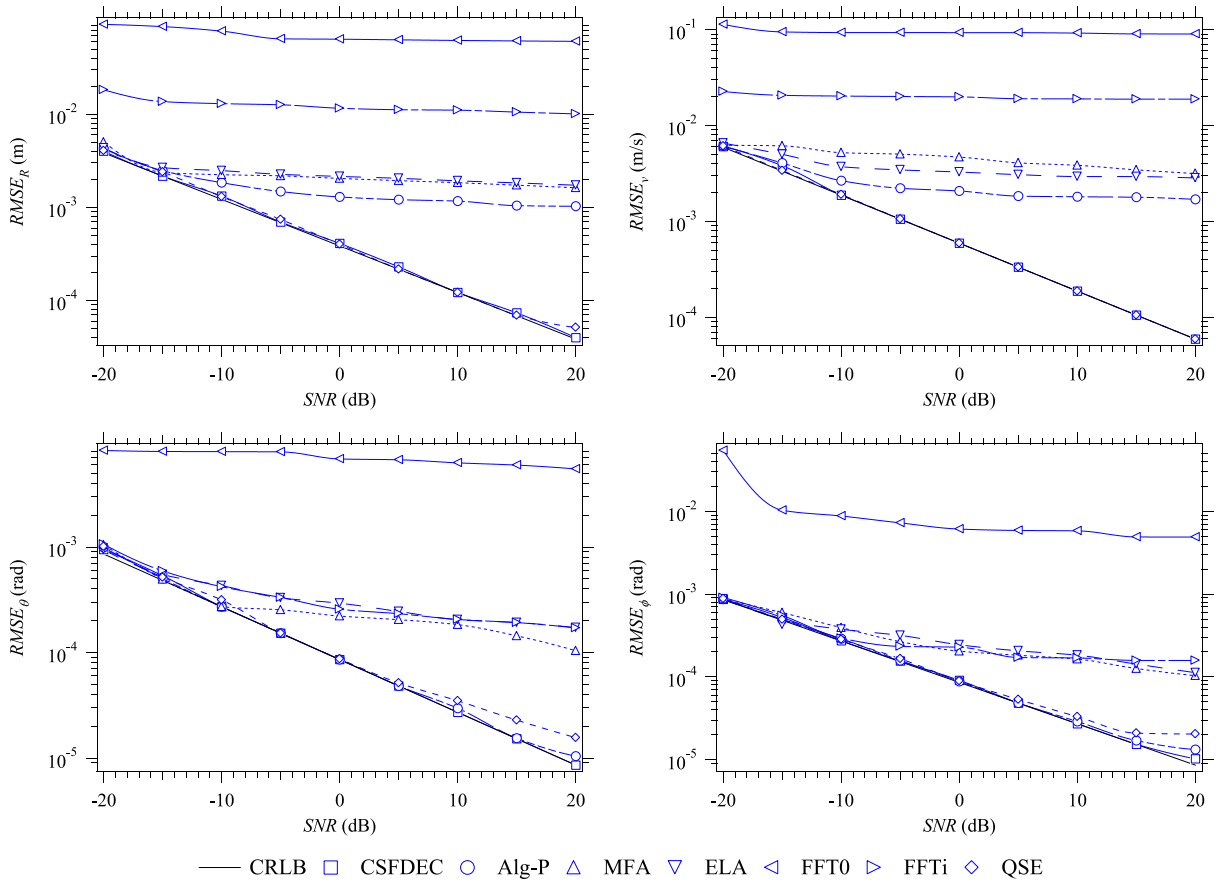

FIGURE 7. Root mean square error performance achieved by the considered embodiments of the DRAEC strategy. The third scenario is considered.

3) The QSE represents the best option in the case of single target. However, if the overall number of targets increases, it is outperformed by the CSFDEC and the Alg-P; this is due to the fact that the CSFDEC algorithm and the Alg-P make use of a serial cancellation procedure.

4) The ELA performs better than the MFA in the considered scenario.

5) The FFT0 and the FFTi are less accurate than all the other techniques.

In Fig. 9, instead, the computational complexity of all the embodiments is represented for a variable number of targets; both the *computational cost*, measured in *mega* FLOPs (MFLOPs), and the *computation time*[25] (CT) are taken into consideration. From this figure, it is easily inferred that:

1) The trend of most of the CT curves is similar and in agreement with that characterising the corresponding curves of the computational cost; the only exception is represented by the CSFDEC, for which the trend of the computational cost appears to be flatter than that of the CT.

2) The slopes of all the curves (i.e., the relative increase in complexity as K gets larger) are similar.

25. These metrics allow us to compare the impact of different 2D estimators available in the technical literature on the overall computational effort required by the DRAEC, since this mainly depends on the complexity of the specific algorithm adopted in its two core blocks.

3) The CT of the Alg-P is very close to that required by the FFT0 and the FFTi; moreover, the last two methods require similar CTs.

4) Even if the complexity of the QSE is similar to that of the Alg-P, the CT of the former embodiment tends to be larger than that of the latter; this is mainly due to the fact their estimators have different initializations. In fact, in the case of the QSE (the Alg-P), the search for K local maxima (for a single maximum) is required.

The results shown in this section evidence that the CSFDEC represents the winning option among the set of considered embodiments, since it achieves the best performance-complexity trade-off.

VII. CONCLUSION

In this manuscript, a novel general strategy to develop sub-optimal methods for the detection of multiple targets and the estimation of their parameters in a MIMO OFDM-based JCAS system has been proposed. This strategy is based on the idea of splitting a complicated optimization problem into a couple of simpler (but interacting) sub-problems. Seven different embodiments of it have been described, their complexity has been assessed and their estimation accuracy has been compared in four different scenarios. Our numerical results, based on synthetically generated data referring

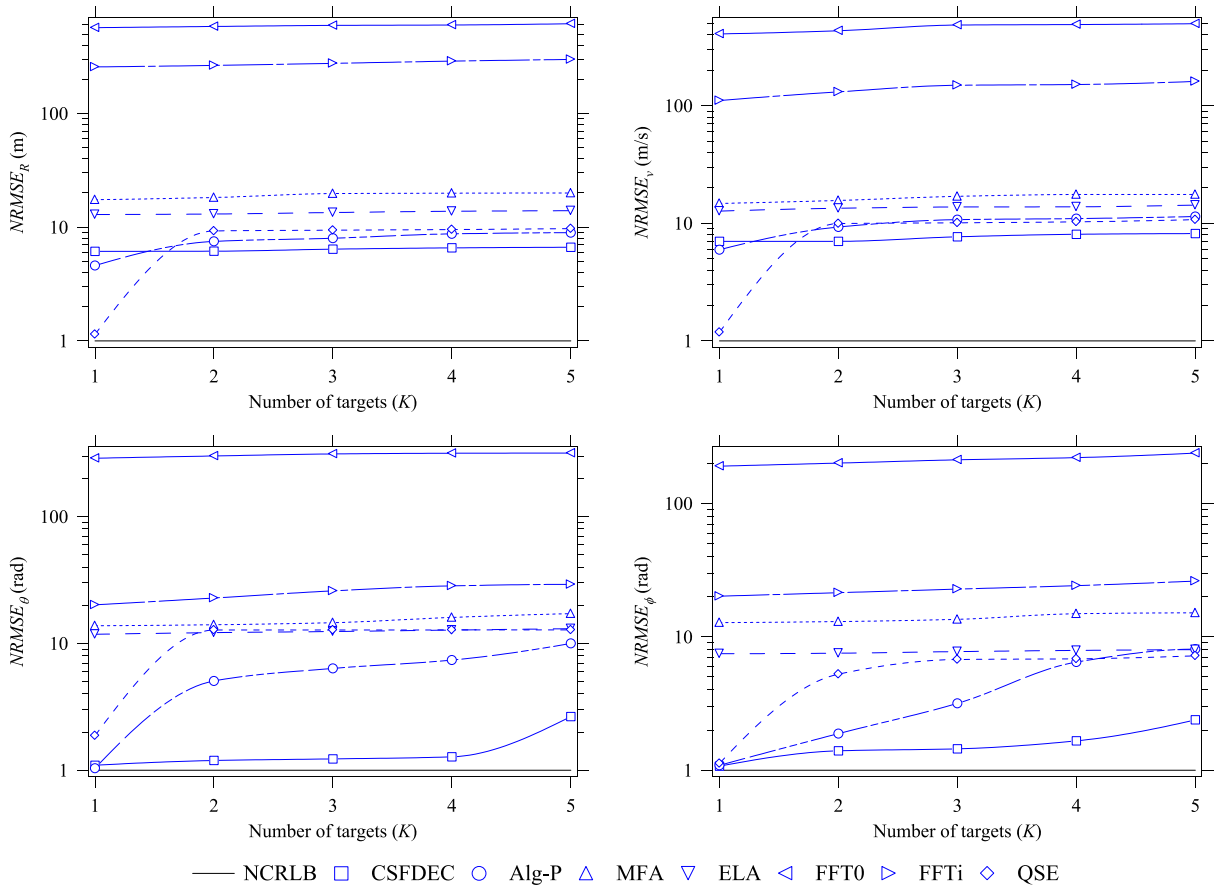

FIGURE 8. Root mean square error performance achieved by the considered embodiments of the DRAEC strategy. The fourth scenario is considered.

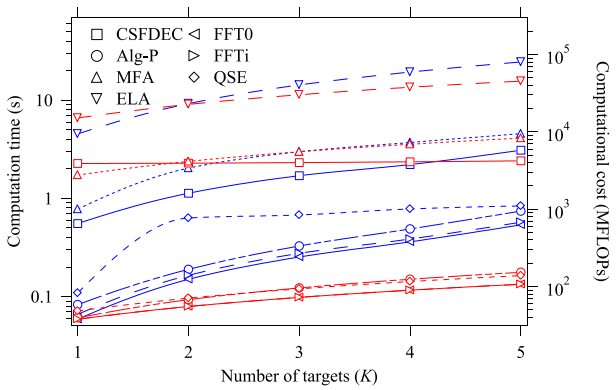

FIGURE 9. ***Computation time*** **(blue lines) and** ***computational cost*** **(red lines) characterizing the analyzed embodiments in the presence of a variable number of targets. The fourth scenario is considered.**

to four distinct scenarios, evidence that all the proposed embodiments perform reasonably well, but may require substantially different computational efforts. Moreover, the estimation accuracy of the majority of the algorithms exhibits a floor as the SNR increases. This phenomenon is due to the lack of an iterative procedure for refining the coarse estimates of the detected targets or to the use of a sub-optimal refinement procedure or to the adoption of a (discretized) search grid.

We believe that our work sheds new light on a complicated technical problem, which plays a key role in the development of future JCAS systems; in fact, it provides an in-depth analysis of the accuracy-complexity trade-off characterizing different solutions to it. In a number of applications, achieving good estimation accuracy represents a fundamental requirement; at the same time, real-time operation is also needed, so that substantial attention must be paid to the computational effort required by the adopted estimation algorithms. All in all, we believe the detection and estimation algorithms based on the strategy we propose can represent good candidates for the processing to be accomplished in OFDM-based 4D radars. Our future work includes the application of the proposed strategy to MIMO JCAS systems employing the *Orthogonal Time Frequency Space* (OTFS) modulation.

APPENDIX

A. CRAMER-RAO LOWER BOUND DERIVATION

Cramer-Rao lower bounds for OFDM-based radar systems have been already derived in [4] and [16], but refer to the estimation of Doppler and range only. In this Appendix, the procedure we followed in the evaluation of the CRLBs for Doppler, range, azimuth and elevation is sketched.

First of all, let us consider the signal model (40), that refers to K distinct targets; the parameters of these targets are collected in the vectors[26]

$$\Gamma \triangleq \left[\gamma_0, \gamma_1, \ldots, \gamma_{K-1}\right]^T, \tag{149}$$

$$\mathbf{F}_D = \left[F_{D_0}, F_{D_1}, \ldots, F_{D_{K-1}}\right]^T, \tag{150}$$

$$\mathbf{F}_\rho = \left[F_{\rho_0}, F_{\rho_1}, \ldots, F_{\rho_{K-1}}\right]^T, \tag{151}$$

$$\mathbf{F}_V = \left[F_{V_0}, F_{V_1}, \ldots, F_{V_{K-1}}\right]^T \tag{152}$$

and

$$\mathbf{F}_H = \left[F_{H_0}, F_{H_1}, \ldots, F_{H_{K-1}}\right]^T. \tag{153}$$

We also define: 1) the trial vectors $\tilde{\Gamma}$, $\tilde{\mathbf{F}}_D$, $\tilde{\mathbf{F}}_\rho$, $\tilde{\mathbf{F}}_V$ and $\tilde{\mathbf{F}}_H$ in a similar way as Γ, $\mathbf{F}_D$, $\mathbf{F}_\rho$, $\mathbf{F}_V$ and $\mathbf{F}_H$, respectively (see (149)-(153)); 2) the vectors $\hat{\Gamma}$, $\hat{\mathbf{F}}_D$, $\hat{\mathbf{F}}_\rho$, $\hat{\mathbf{F}}_V$ and $\hat{\mathbf{F}}_H$, structured like Γ, $\mathbf{F}_D$, $\mathbf{F}_\rho$, $\mathbf{F}_V$ and $\mathbf{F}_H$, respectively, but collecting the ML estimates of all the considered parameters.

The CRLBs we are interested in refer to the ML estimation problem

$$\left(\hat{\mathbf{F}}_D, \hat{\mathbf{F}}_\rho, \hat{\mathbf{F}}_V, \hat{\mathbf{F}}_H, \hat{\Gamma}\right) \triangleq \underset{\tilde{\mathbf{F}}_D, \tilde{\mathbf{F}}_\rho, \tilde{\mathbf{F}}_V, \tilde{\mathbf{F}}_H, \tilde{\Gamma}}{\arg\min} \ \varepsilon(\tilde{\mathbf{a}}); \tag{154}$$

here,

$$\varepsilon(\tilde{\mathbf{a}}) \triangleq \frac{(\mathbf{x} - \tilde{\mathbf{x}})(\mathbf{x} - \tilde{\mathbf{x}})^H}{MNN_TN_R} \tag{155}$$

is a *mean square error* (MSE) referring to the (MNN_TN_R)-dimensional column vector

$$\mathbf{x} \triangleq \Gamma^T \Psi\left(\mathbf{F}_D, \mathbf{F}_\rho, \mathbf{F}_V, \mathbf{F}_H\right) + \mathbf{w} \tag{156}$$

and its useful component

$$\tilde{\mathbf{x}} = \mathbf{x}(\tilde{\mathbf{a}}) = \tilde{\Gamma}^T \tilde{\Psi}. \tag{157}$$

In the last two formulas,

$$\tilde{\mathbf{a}} \triangleq \left[\tilde{\mathbf{F}}_D^T, \tilde{\mathbf{F}}_\rho^T, \tilde{\mathbf{F}}_V^T, \tilde{\mathbf{F}}_H^T, \tilde{\Gamma}^T\right]^T \tag{158}$$

is a $(5K)$-dimensional column vector collecting the trial values of the target parameters, $\mathbf{w}$ is a (MNN_TN_R)-dimensional noise vector, $\tilde{\Psi} = \Psi(\tilde{\mathbf{F}}_D, \tilde{\mathbf{F}}_\rho, \tilde{\mathbf{F}}_V, \tilde{\mathbf{F}}_H)$,

$$\Psi\left(\mathbf{F}_D, \mathbf{F}_\rho, \mathbf{F}_V, \mathbf{F}_H\right) \triangleq \mathbf{A}(\mathbf{F}_D) * \mathbf{B}\left(\mathbf{F}_\rho\right) * \mathbf{C}(\mathbf{F}_V) * \mathbf{D}(\mathbf{F}_H) \tag{159}$$

is a $(MNN_TN_R) \times K$ steering matrix, and $\mathbf{A}(\mathbf{F}_D)$, $\mathbf{B}(\mathbf{F}_\rho)$, $\mathbf{C}(\mathbf{F}_V)$ and $\mathbf{D}(\mathbf{F}_H)$ are $M \times K$, $N \times K$, $N_R \times K$ and $N_T \times K$ matrices, respectively; the kth column (with $k = 0, 1, \ldots, K-1$) of the last four matrices is defined as

$$\mathbf{A}\left(F_{D_k}\right) \triangleq \left[a_0\left(F_{D_k}\right), a_1\left(F_{D_k}\right), \ldots, a_m\left(F_{D_k}\right), \ldots, a_{M-1}\left(F_{D_k}\right)\right]^T, \tag{160}$$

$$\mathbf{B}\left(F_{\rho_k}\right) \triangleq \left[a_0\left(-F_{\rho_k}\right), a_1\left(-F_{\rho_k}\right), \ldots, a_n\left(-F_{\rho_k}\right), \ldots, a_{N-1}\left(-F_{\rho_k}\right)\right]^T, \tag{161}$$

26. The kth element of the vector Γ represents the complex amplitude of the kth target and coincides with the parameter A_k defined in Section VI.

$$\mathbf{C}\left(F_{V_k}\right) \triangleq \left[a_0\left(-F_{V_k}\right), a_1\left(-F_{V_k}\right), \ldots, a_q\left(-F_{V_k}\right), \ldots, a_{N_R-1}\left(-F_{V_k}\right)\right]^T, \tag{162}$$

and

$$\mathbf{D}\left(F_{H_k}\right) \triangleq \left[a_0\left(-F_{H_k}\right), a_1\left(-F_{H_k}\right), \ldots, a_p\left(-F_{H_k}\right), \ldots, a_{N_T-1}\left(-F_{H_k}\right)\right]^T, \tag{163}$$

respectively ($a_z(F_X)$ is defined by (32), with $z = m$, n, q or p, and $X = D$, ρ, V or H if $z = m$, n, q or p, respectively).

If we assume that the elements of the noise vector $\mathbf{w}$ are Gaussian, mutually independent and have zero mean and variance σ_W^2, the CRLBs of all the parameters of interest are represented by the diagonal elements of the matrix

$$\mathbf{V} = \sigma_W^2 \mathbf{F}^{-1}, \tag{164}$$

where

$$\mathbf{F} \triangleq 2\Re\left\{\frac{\partial \tilde{\mathbf{x}}}{\partial \tilde{\mathbf{a}}}\left(\frac{\partial \tilde{\mathbf{x}}}{\partial \tilde{\mathbf{a}}}\right)^H\right\} \tag{165}$$

is the $(5K \times 5K)$-dimensional *Fisher information matrix* computed for the vector $\tilde{\mathbf{x}}$,

$$\frac{\partial \tilde{\mathbf{x}}}{\partial \tilde{\mathbf{a}}} = \left[\bar{\mathbf{A}}, \bar{\mathbf{B}}, \bar{\mathbf{C}}, \bar{\mathbf{D}}, \tilde{\Psi}\right]^T, \tag{166}$$

$\bar{\mathbf{A}} \triangleq [\bar{\mathbf{A}}_0, \bar{\mathbf{A}}_1, \ldots, \bar{\mathbf{A}}_{K-1}]$, $\bar{\mathbf{B}} \triangleq [\bar{\mathbf{B}}_0, \bar{\mathbf{B}}_1, \ldots, \bar{\mathbf{B}}_{K-1}]$, $\bar{\mathbf{C}} \triangleq [\bar{\mathbf{C}}_0, \bar{\mathbf{C}}_1, \ldots, \bar{\mathbf{C}}_{K-1}]$, $\bar{\mathbf{D}} \triangleq [\bar{\mathbf{D}}_0, \bar{\mathbf{D}}_1, \ldots, \bar{\mathbf{D}}_{K-1}]$,

$$\bar{\mathbf{A}}_k \triangleq -\tilde{\gamma}_k\left(\Upsilon_M \odot \mathbf{A}\left(\tilde{F}_{D_k}\right)\right) * \mathbf{B}\left(\tilde{F}_{\rho_k}\right) * \mathbf{C}\left(\tilde{F}_{V_k}\right) * \mathbf{D}\left(\tilde{F}_{H_k}\right), \tag{167}$$

$$\bar{\mathbf{B}}_k \triangleq \tilde{\gamma}_k \mathbf{A}\left(\tilde{F}_{D_k}\right) * \left(\Upsilon_N \odot \mathbf{B}\left(\tilde{F}_{\rho_k}\right)\right) * \mathbf{C}\left(\tilde{F}_{V_k}\right) * \mathbf{D}\left(\tilde{F}_{H_k}\right), \tag{168}$$

$$\bar{\mathbf{C}}_k \triangleq \tilde{\gamma}_k \mathbf{A}\left(\tilde{F}_{D_k}\right) * \mathbf{B}\left(\tilde{F}_{\rho_k}\right) * \left(\Upsilon_{N_R} \odot \mathbf{C}\left(\tilde{F}_{V_k}\right)\right) * \mathbf{D}\left(\tilde{F}_{H_k}\right), \tag{169}$$

$$\bar{\mathbf{D}}_k \triangleq \tilde{\gamma}_k \mathbf{A}\left(\tilde{F}_{D_k}\right) * \mathbf{B}\left(\tilde{F}_{\rho_k}\right) * \mathbf{C}\left(\tilde{F}_{V_k}\right) * \left(\Upsilon_{N_T} \odot \mathbf{D}\left(\tilde{F}_{H_k}\right)\right), \tag{170}$$

and

$$\Upsilon_X \triangleq \left[0, -j2\pi, \ldots, -j2\pi(X-1)\right]^T. \tag{171}$$

for any integer X.

In our work, all the above-mentioned CRLBs have been evaluated numerically on the basis of (164)-(171); in particular, in the computation of $\bar{\mathbf{A}}_k$, $\bar{\mathbf{B}}_k$, $\bar{\mathbf{C}}_k$ and $\bar{\mathbf{D}}_k$, the following choices have been made for any k: 1) the complex gain $\tilde{\gamma}_k$ (corresponding to A_k in Section VI) has been set to unity in all the considered scenarios; 2) the noise variance σ_W^2 has been derived from (146), since the SNR and the amplitudes of the target echoes are known in all the considered scenarios. Moreover, as far as the normalized frequencies $\tilde{F}_{D_k}$, $\tilde{F}_{\rho_k}$, $\tilde{F}_{V_k}$ and $\tilde{F}_{H_k}$ are concerned, the following rules have been followed:

a) $\tilde{F}_{X_0}$ has been set to the expected value $\bar{F}_{X_0}$ of the normalized frequency of the first target (with $X = D$, ρ, V

or H). This choice is motivated by the fact that, in all the considered scenarios, the four normalized frequencies characterizing the first target are uniformly distributed random variables; therefore, $\bar{F}_{X_0} = (F_{X_{\max}} - F_{X_{\min}})/2$ (the values of $F_{X_{\max}}$ and $F_{X_{\min}}$ are provided in Section VI).

b) The other $(K-1)$ frequencies $\{\tilde{F}_{X_k}; k = 1, 2, \ldots, K-1\}$ have been set to $\bar{F}_{X_0} + k\, F_{X_{\text{bin}}}\, F_{X_{\text{res}}}$ for any k; here, $F_{X_{\text{bin}}} = X_{\text{bin}}$ represents the normalized bin spacing between adjacent targets adopted in the considered scenario and $F_{X_{\text{res}}} = 1/Q$, where $Q = M, N, N_R$ or N_T if $X = D, \rho, V$ or H, respectively.

REFERENCES

[1] J. A. Zhang et al., "An overview of signal processing techniques for joint communication and radar sensing," *IEEE J. Sel. Topics Signal Process.*, vol. 15, no. 6, pp. 1295–1315, Nov. 2021.

[2] C. Sturm and W. Wiesbeck, "Waveform design and signal processing aspects for fusion of wireless communications and radar sensing," *Proc. IEEE*, vol. 99, no. 7, pp. 1236–1259, Jul. 2011.

[3] Y. Zhang, Q. Li, L. Huang, and J. Song, "Waveform design for joint radar-communication system with multi-user based on MIMO radar," in *Proc. IEEE Radar Conf. (RadarConf)*, May 2017, pp. 415–418.

[4] P. Kumari, J. Choi, N. González-Prelcic, and R. W. Heath, "IEEE 802.11ad-based radar: An approach to joint vehicular communication-radar system," *IEEE Trans. Veh. Technol.*, vol. 67, no. 4, pp. 3012–3027, Apr. 2018.

[5] K. V. Mishra, M. B. Shankar, V. Koivunen, B. Ottersten, and S. A. Vorobyov, "Toward millimeter-wave joint radar communications: A signal processing perspective," *IEEE Signal Process. Mag.*, vol. 36, no. 5, pp. 100–114, Sep. 2019.

[6] S. H. Dokhanchi, B. S. Mysore, K. V. Mishra, and B. Ottersten, "A mmWave automotive joint radar-communications system," *IEEE Trans. Aerosp. Electron. Syst.*, vol. 55, no. 3, pp. 1241–1260, Jun. 2019.

[7] G. L. Stuber, J. R. Barry, S. W. McLaughlin, Y. Li, M. A. Ingram, and T. G. Pratt, "Broadband MIMO-OFDM wireless communications," *Proc. IEEE*, vol. 92, no. 2, pp. 271–294, Feb. 2004.

[8] M. Jiang and L. Hanzo, "Multiuser MIMO-OFDM for next-generation wireless systems," *Proc. IEEE*, vol. 95, no. 7, pp. 1430–1469, Jul. 2007.

[9] C. R. Berger, B. Demissie, J. Heckenbach, P. Willett, and S. Zhou, "Signal processing for passive radar using OFDM waveforms," *IEEE J. Sel. Topics Signal Process.*, vol. 4, no. 1, pp. 226–238, Feb. 2010.

[10] Y. L. Sit, C. Sturm, and T. Zwick, "Doppler estimation in an OFDM joint radar and communication system," *Proc. German Microw. Conf.*, Mar. 2011, p. 4.

[11] C. Knill, B. Schweizer, S. Sparrer, F. Roos, R. F. H. Fischer, and C. Waldschmidt, "High range and doppler resolution by application of compressed sensing using low baseband bandwidth OFDM radar," *IEEE Trans. Microw. Theory Techn.*, vol. 66, no. 7, pp. 3535–3546, Jul. 2018.

[12] S. Mercier, S. Bidon, D. Roque, and C. Enderli, "Comparison of correlation-based OFDM radar receivers," *IEEE Trans. Aerosp. Electron. Syst.*, vol. 56, no. 6, pp. 4796–4813, Dec. 2020.

[13] J. B. Sanson, P. M. Tomé, D. Castanheira, A. Gameiro, and P. P. Monteiro, "High-resolution delay-doppler estimation using received communication signals for OFDM radar-communication system," *IEEE Trans. Veh. Technol.*, vol. 69, no. 11, pp. 13112–13123, Nov. 2020.

[14] F. Zhang, Z. Zhang, W. Yu, and T.-K. Truong, "Joint range and velocity estimation with intrapulse and intersubcarrier doppler effects for OFDM-based RadCom systems," *IEEE Trans. Signal Process.*, vol. 68, pp. 662–675, 2020.

[15] Y. Liu, G. Liao, Y. Chen, J. Xu, and Y. Yin, "Super-resolution range and velocity estimations with OFDM integrated radar and communications waveform," *IEEE Trans. Veh. Technol.*, vol. 69, no. 10, pp. 11659–11672, Oct. 2020.

[16] R. Xie, D. Hu, K. Luo, and T. Jiang, "Performance analysis of joint range-velocity estimator with 2D-MUSIC in OFDM radar," *IEEE Trans. Signal Process.*, vol. 69, pp. 4787–4800, 2021.

[17] M. L. Rahman, J. A. Zhang, X. Huang, Y. J. Guo, and R. W. Heath, "Framework for a perceptive mobile network using joint communication and radar sensing," *IEEE Trans. Aerosp. Electron. Syst.*, vol. 56, no. 3, pp. 1926–1941, Jun. 2020.

[18] D. Werbunat et al., "Multiplexing of OFDM-based radar networks," in *Proc. IEEE Radar Conf. (RadarConf)*, May 2021, pp. 1–6.

[19] Z. Xu and A. Petropulu, "A bandwidth efficient dual-function radar communication system based on a MIMO radar using OFDM waveforms," *IEEE Trans. Signal Process.*, vol. 71, pp. 401–416, 2023.

[20] A. El Assaad, M. Krug, and G. Fischer, "Distance and vehicle speed estimation in OFDM multipath channels," in *Proc. 21st Int. Conf. Microw. Radar Wireless Commun. (MIKON)*, May 2016, pp. 1–5.

[21] U. K. Singh, R. Mitra, V. Bhatia, and A. K. Mishra, "Target range estimation in OFDM radar system via kernel least mean square technique," in *Proc. Int. Conf. Radar Syst. (Radar)*, Oct. 2017, pp. 1–5.

[22] J. Fink, M. Braun, and F. K. Jondral, "Effects of arbitrarily spaced Subcarriers on detection performance in OFDM radar," in *Proc. IEEE Veh. Technol. Conf (VTC Fall)*, Sep. 2012, pp. 1–5.

[23] Y.-C. Lin, T.-S. Lee, Y.-H. Pan, and K.-H. Lin, "Low-complexity high-resolution parameter estimation for automotive MIMO radars," *IEEE Access*, vol. 8, pp. 16127–16138, 2020.

[24] J. Wang, P. Wang, F. Luo, and W. Wu, "Waveform design and DoA-DoD estimation of OFDM-LFM signal based on SDFnT for MIMO radar," *IEEE Access*, vol. 11, pp. 1348–1358, 2023.

[25] S.-F. Chuang, W.-R. Wu, and Y.-T. Liu, "High-resolution AoA estimation for hybrid antenna arrays," *IEEE Trans. Antennas Propag.*, vol. 63, no. 7, pp. 2955–2968, Jul. 2015.

[26] L. Liu and S. Zhang, "A two-stage radar sensing approach based on MIMO-OFDM technology," in *Proc. IEEE Globecom Workshops (GC Wkshps)*, Dec. 2020, pp. 1–6.

[27] H. Lee and J. Chun, "Virtual array response vector for angle estimation of MIMO radar with a wide-band interleaved OFDM signal," *IEEE Wireless Commun. Lett.*, vol. 25, no. 5, pp. 1539–1543, May 2021.

[28] C. Knill, F. Embacher, B. Schweizer, S. Stephany, and C. Waldschmidt, "Coded OFDM waveforms for MIMO radars," *IEEE Trans. Veh. Technol.*, vol. 70, no. 9, pp. 8769–8780, Sep. 2021.

[29] M. F. Keskin, H. Wymeersch, and V. Koivunen, "MIMO-OFDM joint radar-communications: Is ICI friend or foe?" *IEEE J. Sel. Topics Signal Process.*, vol. 15, no. 6, pp. 1393–1408, Nov. 2021.

[30] V. Popović-Bugarin and S. Djukanović, "A low complexity model order and frequency estimation of multiple 2-D complex sinusoids," *Digit. Signal Process.*, vol. 104, Sep. 2020, Art. no. 102794.

[31] V. Solak, S. Aldirmaz-Colak, and A. Serbes, "Fast and efficient 2-D and K-D DFT-based sinusoidal frequency estimation," *IEEE Trans. Signal Process.*, vol. 70, pp. 5087–5101, 2022.

[32] M. Mirabella, P. Di Viesti, A. Davoli, and G. M. Vitetta, "An approximate maximum likelihood method for the joint estimation of range and doppler of multiple targets in OFDM-based radar systems," *IEEE Trans. Commun.*, early access, May 29, 2023, doi: 10.1109/TCOMM.2023.3280562.

[33] D. Fan et al., "Angle domain channel estimation in hybrid millimeter wave massive MIMO systems," *IEEE Wireless Commun.*, vol. 17, no. 12, pp. 8165–8179, Dec. 2018.

[34] P. Di Viesti, A. Davoli, G. Guerzoni, and G. M. Vitetta, "Novel deterministic detection and estimation algorithms for colocated multiple-input–multiple-output radars," *IEEE Access*, vol. 10, pp. 2216–2255, 2022.

[35] D. Roque and S. Bidon, "Range migration in symbol-based OFDM radar receivers," in *Proc. IEEE 22nd Int. Workshop Signal Process. Adv. Wireless Commun. (SPAWC)*, Nov. 2021, pp. 496–500.

MICHELE MIRABELLA (Graduate Student Member, IEEE) received the B.S. degree and the M.S. degree (both cum laude) in electronic engineering from the University of Modena and Reggio Emilia, Italy, in 2019 and 2021, respectively, where he is currently pursuing the Ph.D. degree. His main research interests lie in the area of joint communication and sensing systems.

PASQUALE DI VIESTI (Graduate Student Member, IEEE) received the bachelor's degree and the master's degree (both cum laude) in electronic engineering from the University of Modena and Reggio Emilia, Italy, in 2016 and 2018, respectively, and the Ph.D. program in "Automotive for an Intelligent Mobility" with the University of Bologna in October 2021. He is currently a Postdoctoral Research Fellow with the University of Modena and Reggio Emilia. His main research interests lie in the area of statistical signal processing and MIMO radars.

GIORGIO M. VITETTA (Senior Member, IEEE) received the Dr.Ing. degree (cum laude) in electronic engineering and the Ph.D. degree from the University of Pisa, Italy, in 1990 and 1994, respectively. He has been a Full Professor of Telecommunications with the University of Modena and Reggio Emilia since 2001. He has coauthored more than 100 papers published on international journals and on the proceedings of international conferences, and has coauthored the book *Wireless Communications: Algorithmic Techniques* (Wiley, 2013). His main research interests lie in the broad area of wireless and wired data communications, localization systems, MIMO radars, and smart grid. He has served as an Area Editor for the IEEE TRANSACTIONS ON COMMUNICATIONS and an Associate Editor for the IEEE WIRELESS COMMUNICATIONS LETTERS and the IEEE TRANSACTIONS ON WIRELESS COMMUNICATIONS.

Open Access funding provided by 'Università degli Studi di Modena e Reggio Emilia' within the CRUI CARE Agreement